Reference Atmosphere for Mercury
Final Report
NAG5-6998
Rosemary M. Killen

The objectives of this three year proposal are : (1) to calculate the likely diffusive flux of Ar and He from the interior of Mercury for representative crustal compositions (2) compute a reasonable estimate of the fractional escape flux of photoions for the likely range of field conditions and (3) to calculate the capture rate of solar wind ions into the atmosphere. The morphology of the magnetosphere in response to the solar wind and the IMF is the crucial boundary condition for the flux of ions to the surface. We have tackled problem (1) using a multipath diffusion code (Lee and Aldama, 1992), and problems (2) and (3) using a combination of MHD and kinetic plasma dynamics.

Task 1: We first modified the multi-path diffusion code (Lee and Aldama, 1992) to include radiogenic production of ^{40}Ar. Argon concentrations inside the grains are assumed to be zero at the start of the run, and to increase with radiogenic production. The Mercury application is more complicated than the application for which the code was written because long time scales and many different spatial scales are involved. For instance, there are high diffusivity paths inside grains due to dislocations in crystals, defects, melt inclusions, microcracks, and dislocations. There are also grain boundaries and larger cracks. Thus, we have a multipath problem but only a two path diffusion code. Therefore we have to parameterize the first part of the diffusion problem (that inside the grain) taking advantage of previous work. The exchange coefficients, which determine the exchange of diffusant from the low diffusivity paths to the high diffusivity paths, and vice versa, are dependent on the density of defects. Since we don't know the defect density, we simply have to assume a range of values from terrestrial samples. We must also use temperature dependent diffusion coefficients, since at sufficiently low temperatures the only way the argon can escape is through volume. In year two we modified the multi-path diffusion code for the conditions at Mercury, and set up a fractal model for the regolith and megaregolith.

Tasks 2 and 3. We attacked the second and third problems with two different approaches, a MHD approach and a kinetic approach. The results of the first approach were presented at the spring AGU meeting (Killen *et al.*, 1999), and the fall AGU meeting. In order to estimate the flux of solar wind ions to the surface we used a modified version of the Toffoletto-Hill (1993) model of the open magnetosphere. The code was scaled for Mercury's field strength and for the expected lack of a ring current, and for the inclusion of the x component of the IMF (which is larger at Mercury than at the Earth) (Sarantos, 2000). Pat Reiff and her students A. Urquhart and M. Sarantos worked with us on this model. A major advance has been to include the x (radial anti-sunward) component of the interplanetary magnetic field.

The boundary conditions for the magnetosphere are the solar wind density and speed, and the magnitude and direction of the IMF. A tomographic inversion of the interplanetary scintillation has been used to infer the solar wind in regions inaccessible to in-situ observations (Hick and Jackson 1994; Jackson *et al.,* 1998). Prior to September, 1994, IPS scintillation level data are available from the radio array in Cambridge, UK, as well as IPS velocity data from the Solar-terrestrial Laboratory (STELab) operated by the University of Nagoya, Japan. Since mid-1997 we have both IPS scintillation level and velocity data available from STELab. For the June, 1994, and November, 1997, dates for which Mercury sodium observations are reduced, we have obtained both solar wind density and velocity information from the new time-dependent algorithm (Figs. 4, 5).

In year two the magnetosphere model was updated to consider the x component of the IMF and was further scaled to match the Mariner 10 measurements. Since we don't know the IMF at Mercury, this is left as a free parameter, however we now have a commitment from Thomas Detman to work with us to determine the IMF at Mercury. The magnetosphere model was used to compute the locus of open field lines to the surface. This work was presented at the spring AGU meeting (Killen *et al.,* 1999a); and further progress was presented at the fall AGU meeting (Killen *et al.,* 1999b).

In year two a code was written to compute the three-dimensional source and loss rate for ion and electron sputter, photon stimulated desorption and impact vaporization. Impact vaporization is based on a parameterization by Melosh (1989). Radiation pressure was parameterized as a function of true anomaly angle and orbital distance. Preliminary results were presented at the October DPS meeting, and a paper was published (Killen *et al.,* 2001).

Accomplishments for Year 3

I. Magnetosphere model and ion trajectories

Our goals for year 3 were to run the magnetosphere models for two ground based sodium D data sets, to compute a comprehensive model of the exosphere using what we have learned about production and loss, and to publish the results of the neutral source code for sodium. We planned to refine the ion trajectory analysis to handle the heavy ions as a perturbation. These goals have been accomplished (Killen *et al.,* 2001; Sarantos, 2002; Sarantos and Killen, 2002). A follow up paper will be published this summer (2002). We have modeled the magnetosphere and run ion trajectories to determine the loss rates of photoions. These have been published (Sarantos, 2002; Killen and Sarantos, 2002) and a follow-up paper is in preparation comparing the various species. Follow-up work is funded under a new project.

II. Diffusion of argon and argon atmosphere.

Our goal was to run the diffusion code for Ar loss to the atmosphere, and subsequently to use the code to consider loss of He. The results were trained to agree with measured Ar densities at the moon. In year three we planned to investigate the ability of poleward ice

deposits to store and release Ar in an episodic fashion, and calculate a best guess atmosphere, including Na, K, Ar, Ne, and He. This will be done both from below, with diffusion into the atmosphere, and from above with solar wind capture and loss by ionization. These goals have been met (Killen, 2002). Our results for argon are (1) that the argon atmosphere of Mercury is probably no more dense than that at the moon, and that such an atmosphere can be supplied from the upper megaregolith (upper 25 km) and not from great depth (100 km) as predicted by Hodges. We believe that the argon atmospheres may be correlated with shallow moonquakes and that the same behavior should be seen at Mercury. The episodic release from polar ice is in preparation.

References

Asai, K, M. Kojima, M. Tokumaru, A. Yokobe, B.V. Jackson, P.L. Hick, and P.K. Manoharan, Heliospheric tomography using interplanetary scintillation observations, 3.Correlation between speed and electron density fluctuations in the solar wind. *Journ. Geophys. Res.* **103**, 12049, 1998.

Hick, P. and B.V. Jackson, Solar Wind Mass and Momentum Flux Variations at 0.3 AU, *Adv. Sp. Res.*, **14**, 139, 1994.

Jackson, B.V., P.L. Hick, and A. Yokobe, Heliospheric tomography using interplanetary scintillation observations, 1. Combined Nagoya and Cambridge data. *Journ. Geophys. Res.* **103**, 12049, 1998.

Lee, J.K.W. and A.A. Aldama, Multipath Diffusion: a General Numerical Model *Computers in Geosciences*, **18**, 531-555, 1992.

Melosh, H.J. *Impact Cratering a Geologic Process*. Oxford Univ. Press. Oxford, 1989.

Killen, R., B. Giles, S. Curtis, P. Reiff, A. Urquhart, B. Jackson, and A. Potter, Mercury's Sodium Exosphere: A remote sensor of CME dynamics? AGU spring meeting, Boston, 1999.

Toffoletto, F.R. and T.W. Hill, A nonsingular model of the open magnetosphere. *Journ. Geophys. Res.* **98**, 1339-1344, 1993.

Sarantos, M. *An Open Magnetosphere Model for Mercury*, Masters Thesis, Rice University, Feb. 2000.

I

Publications resulting from this grant

A. Papers Presented at Scientific Meetings and Colloquia

Killen, R.M., B. Giles, S. Curtis, P. Reiff, A. Urquhart, B. Jackson, and A. Potter, Mercury's Sodium Atmosphere: A Remote Sensor of Solar CME Dynamics? AGU Spring Meeting, 1999a.

Killen, R.M., B. Giles, P. Reiff, B. Jackson, and A. Lukyanov, Space Weather at Mercury. AGU Fall Meeting Dec. 13-17, San Francisco, CA, 1999b.

Killen, R.M., B. Giles, A.E. Potter, B.V. Jackson, J. Linker and Z. Mikic, Mercury Sodium Atmosphere, Magnetosphere and Solar Wind. *Bull. Am. Astron. Soc.*, **31#4**, 1102, 1999.

Killen, R.M. and T.H. Morgan, Argon Atmosphere: Implications for structure and composition of Mercury's crust, Proceedings of the Mercury conference, Chicago, Oct. 4-5, 2001.

Killen, R.M., T. Bida, M. Sarantos, and D. Boice, Modeling Mercury's Calcium Exosphere, *Proceedings of the European Geophysical Society Meeting*, Nice, France, April 21-26, 2002.

Sarantos, M. and R.M. Killen, Ion Trajectories in Mercury's Magnetosphere, *Proceedings of the European Geophysical Society Meeting*, Nice, France, April 21-26, 2002.

Killen, R.M., Space Weather at Mercury, Invited talk at COSPAR, Oct.. 17 - 19, 2002.

B. Publications in refereed journals

Killen, R.M., A.E. Potter, P. Reiff, M. Sarantos, B.V. Jackson, P. Hick, and B. Giles, 2001. Evidence for Space Weather at Mercury, *J. Geophys. Res.* **106**, 20509-20525.

R.M. Killen, 2002. Source and Maintenance of the Argon Atmospheres of Mercury and the Moon, *Meteoritics and Planetary Science*, in press.

Sarantos, M. 2002. *A model for magnetosphere-exosphere interaction at Mercury.* Ph.D. Thesis, Rice University, Houston, Texas.

Sarantos, M., P.H. Reiff, T.W. Hill, R.M. Killen and A.L. Urquhart, 2001. A Bx-interconnected magnetosphere model for Mercury, *Planetary and Space Science* **49**, 1629 - 1635.

Source and Maintenance of the Argon Atmospheres of Mercury and the Moon

R.M. KILLEN

Southwest Research Institute, P.O. Drawer 28510, 6220 Culebra Road, San Antonio, Texas 78228-0510

rkillen@swri.edu

Abstract-We propose that argon-40 measured in the lunar atmosphere and that in Mercury's atmosphere is due to current diffusion into connected pore space within the crust. Higher temperatures at Mercury, along with more rapid loss from the atmosphere, will lead to a similar or smaller column abundance of argon at Mercury than at the Moon, given the same crustal abundance of potassium. Because the noble gas abundance in the Mercurian atmosphere represents current effusion, it is a direct measure of the crustal potassium abundance. We assume a fractal distribution of distance to a connected pore space, with the shortest distance increasing with depth. Given this "rock size" distribution, we show that the diffusive flux is not a unique function of temperature. Even though the diffusion coefficient is an exponential function of temperature, the flux to the surface is fairly insensitive to the temperature.

INTRODUCTION

We consider diffusion of radiogenic argon from the regolith and megaregoliths of Mercury and the moon to the atmosphere, and its subsequent escape via ionization and entrainment in the solar wind. We consider diffusion and effusion of radiogenic argon from its source in the megaregolith to the surface, and loss from the atmosphere. We will not consider diffusion in the atmosphere itself, leading to a redistribution of argon in the atmosphere as considered by Hodges (1975), nor do we consider the possibility of argon trapping in the polar regions, previously considered by Hodges (1980). These topics are beyond the scope of the present paper. Our estimates of argon column in the atmosphere and of argon loss rates are strictly planet-wide and daily averages.

We assume that the argon gas diffuses outward to a connected pore space, from which it can reach the surface by Knudsen flow. We assume a fractal distribution of rock sizes, and we assume that the smallest rock size in the distribution increases with depth, illustrated in Figure 1. For the purpose of this paper, the definition of a rock radius is the shortest distance from the center of the "rock" to a pore space which is connected to the surface via pathways that are open either all of the time or at reasonably short time intervals. We show that because the flux to the surface from the "rock unit" depends not only on the temperature and time but also on the rock size, the maximum flux from an ensemble of rock sizes may not correspond to the highest temperature.

^{40}Ar in the atmospheres of the planets is a measure of potassium abundance in the interiors, since ^{40}Ar is a product of radiogenic decay of ^{40}K by electron capture with the subsequent emission of a 1.46 MeV γ-ray. ^{36}Ar is only 1/15 as abundant in the lunar atmosphere as ^{40}Ar, indicating that captured solar wind argon is not a large fraction of the atmospheric argon. We expect it to be even less important at Mercury due to the intrinsic planetary magnetic field. Although the ^{40}Ar in the earth's atmosphere is expected to have accumulated since the late bombardment, ^{40}Ar in the atmospheres of Mercury and the Moon is eroded quickly by photoionization and electron impact ionization, followed by

pick-up by the interplanetary magnetic field. We will assume that 50% of the newly created ions are recycled to the surface (Manka and Michel, 1971), although we argue that a larger percentage may be recycled at Mercury (Sarantos, 2002).

We reconsider the source and loss processes for the argon atmospheres of Mercury and the Moon in order to investigate what these atmospheres tell us about the structure and composition of the megaregolith. Argon is especially important because it does not engage in chemistry. In order to interpret measurements of argon in Mercury's atmosphere, we must have a model including sources from the interior and loss from the atmosphere. Our model will be trained on the Moon, where data from in-situ measurements are available from instruments left on the surface by the Apollo 17 astronauts.

First we consider production of ^{40}Ar from ^{40}K, and its diffusion to the surface. It is well known that the noble gases readily diffuse through the rocks in which they are found because of their unique qualities, and diffusion of argon has been well studied (e.g. Mussett, 1969). However, detailed calculations of diffusion of argon through a regolith and megaregolith have not been published previously. We assume a fractal distribution of effective unit sizes, and we assume that the minimum unit size increases with depth. We fit the results of numerical calculations of diffusion of argon to the surface of spheres of various sizes to an analytic function so that we can integrate this function over the distribution of radii and over depth.

Argon was measured on the lunar nightside by the Apollo Lunar Mass Spectrometer Package (ALSEP) carried by Apollo 17 (Hoffman et al., 1973). The dayside measurements were contaminated by outgassing from the Apollo Lander and astronauts, and were not useable. The density of ^{40}Ar at the lunar surface is $<10^2$ at night to 10^5 at the equator at sunrise, with a scale height of about 50 km (Hodges, 1975; Manka and Michel, 1973). The average rate of effusion of ^{40}Ar from the lunar interior was estimated to be between 790 - 1581 atoms cm^{-2} s^{-1} (corresponding to a global average column of 1.3 - 2.7 x10^9 atoms cm^{-2}) with a most probable value of 1154 atoms cm^{-2} s^{-1} (Hodges and Hoffman 1974). Manka and Michel (1971) estimated that the steady-state ^{40}Ar concentration in the lunar atmosphere may be $10^2 - 10^3$ cm^{-3}.

The lunar atmospheric argon abundance appears to be consistent with episodic release. Three of the four argon release events observed by the Apollo 17 mass-spectrometer were correlated with shallow moonquakes (Hodges and Hoffman, 1974; Hodges, 1977). The global release rates in 1973 were 3.5 x10^{21} (s^{-1}) in February, 6x10^{21} in March, 3.7 x10^{21} in June, and 2 x10^{21} in August, and appear to be correlated with seismic activity measured by the ALSEP Lunar seismic network (Hodges, 1977; Nakamura et al., 1974). These seismic events were given as evidence for an episodic opening of deep fractures or vents in which the argon could be released to the surface. An alternative hypothesis was advanced that time variations in the atmospheric argon were due to release of argon temporarily trapped in lunar cold traps, where ^{40}Ar could be tapped at temperatures < 70 K for a year or more at latitudes > 75° (Hodges, 1980). Our results are consistent with the proposal that shallow moonquakes release argon (Binder, 1980). Shallow moonquakes redistribute the open pore volume, so that previously open pore space may become closed

and new pores may become open to the surface. In this way the upper megaregolith can be degassed.

^{40}Ar escapes from the Moon at a rapid rate: 3-6% of the total ^{40}Ar production rate or 12% of the rate if K is confined to depths less than 25 km. K should be preferentially placed in the upper crust as a result of early differentiation, resulting in a potassium abundance of 300< [K] <600 ppm in the upper 25 km (Taylor and Jakes, 1974). Because at the time there appeared to be little evidence for deep fracturing of the lunar crust, Hodges concluded that ^{40}Ar could not be released from lunar rocks by diffusion, and that a molten source region at great depth was required (Hodges, 1977). Following the measurement of argon in the lunar atmosphere, with global loss rates < $2x10^{21}$ atoms s^{-1} (5269 atoms cm^{-2} s^{-1}), the hypothesis was advanced that radiogenic gases were released from a semi-molten asthenosphere in which they were trapped to depths of 600 - 1000 km. Hodges (1980) concluded that the source of the atmospheric argon must be localized hot regions.

Assuming a crustal potassium abundance of 300 ppm (the average of mare basalts), the Hoffman et al. (1973) measurements require equilibrium between the argon production in the upper 9 km of the Moon ($1.135x10^{-3}$ cm^{-3} s^{-1}) and its loss. Hodges et al. (1973) conclude that this loss rate and the observed time variability requires argon release through seismic activity, tapping a deep argon source. Turcotte and Schubert (1988) postulate that the Moon may be quite porous to this depth.

We propose that the current effusive flux of argon into the atmospheres of Mercury and the Moon is consistent with diffusion from a highly fractured crust, but, contrary to the Hodges' theory outlined above, release from great depth during seismic events is not necessary to maintain the observed atmosphere of the Moon. Episodic release of argon is consistent with the opening of connected pore space to the surface, which may become closed during quiet episodes. We believe that episodic release correlated with shallow Moonquakes is more consistent with a source in the upper 25 km, not at great depth where argon may have been released to an asthenosphere above the closure temperature. The overpressure serves to effectively close pores at greater depths than about 25 km on the moon (Heiken et al., 1991).

SOURCE PROCESSES
Diffusion
We first train our model to produce the global average argon abundance in the lunar atmosphere. We will examine the possibilities of sustaining an argon atmosphere by diffusion from the upper 10 km of crust, and subsequently by effusion to the surface. We do not consider redistribution of argon in the atmosphere, condensation at night or freezing out at the poles. These details have been considered for the moon by Hodges (1975; 1980).
We have used a multipath diffusion code (Lee and Aldama, 1992) to numerically calculate the diffusion of argon. The θ method central-difference Crank-Nicolson method is used. This multipath diffusion code was written to solve the diffusion equations for a system in which two diffusion paths with different diffusion rates are possible, with an exchange between the two. We are using the code to simulate radiogenic production of

^{40}Ar from ^{40}K, with subsequent diffusion of ^{40}Ar. The diffusion rate for ^{40}K is assumed to be zero, with the exchange rate equal to the radiogenic production rate. We have assumed spherical rock units, the diameter of which is the distance between connected pore spaces. After diffusion to a pore space the argon is assumed to diffuse to the planet's surface by Knudsen flow, a process which is so rapid in comparison with diffusion that it can be assumed to be instantaneous. The diffusion of argon has been reviewed by Mussett (1969). Diffusion rates are very sensitive to temperature, mineral type and physical condition of the mineral.

The diffusion equations are

$$\frac{\partial \xi}{\partial t} = \nabla \left(D_1 \nabla \xi \right) - K_1 \xi - K_2 \omega \tag{1}$$

$$\frac{\partial \omega}{\partial t} = \nabla \left(D_2 \nabla \omega \right) + K_1 \xi + K_2 \omega \tag{2}$$

where ξ and ω are the concentrations in the low and high diffusivity paths, respectively; ξ = concentration of potassium, ω = concentration of argon, K_1 is the exchange rate of argon from the potassium cell, and K_2 is the exchange rate of potassium to the argon cell: $\xi_o = 1$, $\omega_o = 0$, $D_1 = 0$, $K_2 = 0$. In this case D_1 is zero, which means that potassium does not diffuse out of the cell: the low diffusivity path only contains potassium. In this way we allow the source argon atoms to leak out of path 1 at an exchange rate equal to the argon production rate. The potassium is depleted by production of argon and calcium.

Because of uncertainties in mineral type, we will assume that the diffusion coefficient for the lunar regolith is (a) 10^{-19} cm^2 s^{-1}, appropriate for orthoclase at 275 K (extrapolated from measurements by Brandt and Bartnitskiy (1964)), or (b) 10^{-24} cm^2 s^{-1}, appropriate for anorthite at 275 K (from measurements by Fechtig et al. (1960)). Because the diffusion coefficients for orthoclase minerals were only measured for temperatures above 400 C, their extrapolation to 275 K is extremely uncertain. However, we are sure that 10^{-19} cm^2 s^{-1} is an upper limit to the diffusion coefficient for the Moon. That for Mercury is taken as 10^{-15} cm^2 s^{-1}, assuming anorthite at 450 K (Mussett, 1969 after Fechtig et al., 1960).

We assume a fractal distribution of unit sizes, where a unit is a cohesive grain or rock through which the argon must diffuse to reach a connected pore space. The unit may be a grain, a rock or a larger structure. Therefore the diffusion coefficient does not strictly correspond to grain boundary or volume diffusion. However, argon is most likely to reside in the grain boundary region because potassium is an incompatible element. The fractal dimension is assumed to be 2.5, consistent with projectile fragmentation of quartzite or basalt (Turcotte, 1997). The smallest unit at the surface is 30 μm, consistent with the grain size and distribution measured for the lunar regolith (Heiken et al., 1991). The smallest unit increases with depth, z, as $z^{0.8}$. In other words the smallest unit at depth, z, is $r_0(z)=0.003z^{0.8}$ cm. We integrate to a depth of 25 km, where the connected pore space is effectively cut off by pressure (Heiken et al., 1991).

Results of Diffusion Calculations

We solved for diffusion of radiogenic ^{40}Ar from spherical units of radius, a, given diffusion coefficient, D, using the multipath diffusion code (Lee and Aldama, 1992). These results were validated by comparison with the analytic solution for the ratio of the argon remaining in a sample to the potassium in the sample (Wasserburg, 1957),

$$\frac{^{40}Ar}{^{40}K} = \left(\frac{R}{1+R}\right)\left[-1+\left[6\frac{d^2}{\pi^2}\left[\sum_{m=1}^{1000}\frac{\exp\left[x\left[1-\left(m^2\frac{\pi^2}{d^2}\right)\right]\right]}{\left(d^2-\pi^2 m^2\right)m^2}\right]-3\frac{\cot(d)}{d}+\frac{3}{d^2}\right]\right] \quad (3)$$

where R is the branching ratio to the production of ^{40}Ar (0.1048), and $d^2=\lambda a^2/D$. The decay rate, λ, is 7.833×10^{-10} per year, and $x=\lambda t$. We have taken $t=3.1$ billion years, assuming that diffusion begins after the time of the heavy bombardment. The results agreed with our numerical solution.

In order to integrate the flux over the size distribution and over depth, we fit the flux of argon per unit volume calculated with the numerical diffusion code to a function, F(r), written as a matrix equation:

$$F(r) = c[S]\left[\begin{array}{c} 1+\exp[-(\frac{r-\mu}{\alpha})^\gamma]\left(\frac{r-\mu}{\alpha}\right)^{\frac{r}{\gamma}} \\ \frac{1}{1+r} \end{array}\right]. \quad (4)$$

where r is the radius, S is a matrix of constants, μ, α and γ are parameters of the Weibull distribution, and c is the number of ^{40}K atoms per cubic cm x 10^{-18}. This was done using Mathcad. We integrated this function over a fractal size distribution of units and over depth to 25 km to obtain flux to the surface. Knudsen flow to the surface in connected pore space is assumed to be instantaneous because our calculations showed it to be orders of magnitude faster than diffusion. The values of matrix [S] and the parameters to equation 4 are given in Table I for log (D)= -15, -19 and -24, respectively. This fit is not exclusive to Mercury or the moon but is only a function of the diffusion coefficient.

TABLE 1. Values for analytic fit to diffusive flux

log D	S1	S2	α	μ	γ
-15	0.255	-20.652	15	0.001	1.0

| -19 | 0.265 | -0.634 | 1.5 | 0.001 | 0.6 |
| -24 | 0.305 | -0.201 | 0.11 | 0.001 | 0.52 |

The constant, C, is 1.5×10^{-3}, the number of ^{40}K atoms per cubic cm $\times 10^{-18}$. The factor 10^{-18} was not included in the matrix $[S]$ multiplying the flux, $F(x)$. We have used lunar abundance of potassium in the crust, 300 ppm, and a density of 2.6 g cm^{-3}. The results can be scaled to abundance and density values as found for the Mercurian crust.

Whereas the efflux of a non-radiogenic element will peak at a given rock radius, after which the flux declines for larger rock sizes, the efflux of a radiogenic element, measured per unit volume, will reach an asymptotic value at a given radius, after which it remains constant. In this case the important parameter is the radius below which negligible flux is obtained. For units smaller than the minimum, the flux at the current time is the current production rate. In other words, very small grains degas so rapidly that the current flux can be assumed to be equal to the current production rate. For larger grains, the current flux is the integral of the flux over the volume of the unit. At a given time and diffusion coefficient, that flux will be a maximum for some optimal unit size. For this reason the maximum flux will not correspond to the highest temperature.

For radiogenic production, the flux reaches an asymptotic value for large radii at a given time, in contrast with a system in which a finite amount of diffusant initially in the sample diffuses out leaving the sample devoid of diffusant. For a given diffusion coefficient there is a minimum size below which no appreciable flux is given by the equation. Below this size the current flux equals the production rate. The flux out as a function of unit size is shown in Figure 2 for $D=10^{-19}$ cm^2 s^{-1} and in Figure 3 for $D=10^{-15}$ cm^2 s^{-1}. A comparison of Figures 2 and 3 will help the reader to understand why the diffusive flux is not a monotonic function of D. For small rock units, the flux may be greater for small values of D than for large values of D.

The functions, $F(x)$, were integrated over the fractal distribution of unit sizes with fractal dimension 2.5 and over depth, z, to a depth of 25 km. We assume that the pore spaces are closed below 25 km. Note that the limiting flux, if all of the current argon production in the top 25 km were currently being supplied to the surface is 9019 atoms cm^{-2} s^{-1}.

Moon–Given $x_0(z)=0.003$ $z^{0.8}$cm, we conclude that the current flux of argon for $D=10^{-19}$ cm^2 s^{-1} is 990 atoms cm^{-2} s^{-1}, and that for $D=10^{-24}$ cm^2 s^{-1} is 1448 atoms cm^{-2} s^{-1}. These values are within the limits to the flux estimated to be required by ALSEP measurements of lunar argon (Hodges, 1975), and about one third of the flux estimated during the lunar seismic event of August 1973. The lunar crustal temperature to 25 km is within the range of values consistent with $-24 < \log (D) < -19$, and the measured atmospheric argon is consistent with the flux derived for diffusion coefficients in this range with a fractal distribution of unit sizes. The flux is not very sensitive to the exact diffusion coefficient in this range for our fractal distribution of sizes because all diffusion regimes give the same limiting flux for both small and large unit sizes. There will be some size in between for which the maximum pulse of argon from the interior will be reaching the pore space at the current epoch.

Mercury- The measurement of argon in Mercury's atmosphere by Mariner 10 was inconclusive. An upper limit for the argon abundance in the Mercurian atmosphere was obtained by the UVS spectrometer onboard Mariner 10 (Broadfoot *et al.*, 1976). The subsolar surface abundance of argon is certainly $< 6.6 \times 10^6$ (Shemansky 1988). Assuming a temperature of 450 K, this gives a column abundance of $<1.6 \times 10^{13}$, which would imply that Ar may be the most abundant species in the Mercurian atmosphere. However, this value is an upper limit based on the sensitivity of the UVS instrument. With a photoionization lifetime of about 8 days for quiet sun, aphelion (0.46 AU), or as short as 3.5 days for active sun with Mercury at perihelion (0.306 AU) (using rates from Huebner *et al.*, 1992), any argon in the atmosphere would represent current effusion rates. Some argon ions will become entrained in the solar wind, but some will re-impact the surface of the planet. The escape flux of argon ions from Mercury's magnetosphere is an open question since the degree to which the magnetosphere is open to the solar wind is unknown (Luhmann *et al.*1998; Kabin, 2000; Sarantos *et al.* 2001; Sarantos, 2002). The fraction of argon ions that escape from Mercury is certainly less than that at the Moon, estimated to be about half the ionization production (Manka and Michel, 1971).

If $D=10^{-15}$ cm^2 s^{-1}, the current flux to the surface, given the same fractal distribution of unit sizes assumed above, is 1830 atoms cm^{-2} s^{-1}. In this case 70% of the flux comes from the upper 3.5 km, and corresponds to the current production. We have assumed that the K abundance is 300 ppm. These results are summarized in Table 2. Note that the flux does not vary monotonically with D because we have assumed a fractal distribution of rock unit sizes. The total flux is given by an integral over the size distribution of rock units and over depth. A comparison of Figures 2 and 3 illustrates how the flux varies with rock unit size at two different values of D. Because the flux at Mercury (D=10^{-15} cm^2 s^{-1}) is mostly dependent on the potassium abundance, and less dependent on temperature, the argon in the atmosphere will be a simple measure of potassium abundance in the crust.

In contrast with the Moon, the lifetime of argon at Mercury is only about 3.5 days at perihelion or 8 days at aphelion, giving a total column abundance of about 5×10^8 – 1.2×10^9 atoms cm^{-2} if the flux is 1830 atoms cm^{-2} s^{-1} (Table 2). This is considerably less than the upper limit given by the Mariner 10 UV spectrometer results. Recycling of half of the argon ions would increase the above estimates by 20% as shown in Appendix II.

TABLE 2. Argon flux estimated as a function of diffusion coefficient.

Log (D)	Flux (atoms cm^{-2} s^{-1})
-15	1830
-19	990
-24	1448

Effusion
Argon easily escapes from a melt, and would become trapped in pockets, from which it could effuse to the surface if cracks open. Chemical decomposition and melting are important at high temperature. The closure temperature (the apparent temperature at

which Ar is retained in a laboratory sample) for K-Ar in K-feldspar is 440 - 640 K (Lovera et al., 1989; Hodges, 1991), within the range expected for the regolith and upper crust of Mercury. However, the upper 100 km of the Moon is expected to be under 350 K, and will be below the closure temperature. A wide range of closure temperatures is indicative of multiple diffusion domains, also discussed above.

The thrust faults causing active Moonquakes have a depth of 300 m to 3.5 km (Binder, 1980) and thus would episodically connect open pore space to the surface. The argon having diffused out of the crystalline lattice or grain boundary regions into pore spaces would thus episodically be released to the surface through effusive flow, which is instantaneous on timescales of interest here. Although grinding and melting directly adjacent to the fault will release argon directly from the rock, fracturing of large volumes of rock farther from the fault itself will release significant amounts of ^{40}Ar. It is this process which is important in opening the connected pore spaces and releasing argon which is already in pore spaces and voids.

ATMOSPHERIC ESCAPE

Argon is gravitationally bound on both Mercury and the Moon, and ionization losses dominate over Jeans escape. Argon atoms are mainly lost by photoionization and secondarily by electron impact ionization. At the Moon about half of these ions will return to the surface, where most will become implanted (Manka and Michel, 1971). First we look at the effect of ion implantation on the net flux of argon from the crust and regolith. We assume that the argon ions are implanted into rock units of radius, a. Then we assume that the implantation can be treated as a source in a similar way as the radiogenic source, but with a different source rate given by the implantation rate.

The number of argon atoms in a sphere of radius, a, with volume, V, at quasi-equilibrium with a concentration of ^{40}K, C_k, is (Mussett, 1969)

$$n = \frac{V \cdot \lambda \cdot C_k \cdot a^2}{15D}$$

(5)

where λ is the radiogenic decay rate of ^{40}K, and D is the diffusion coefficient. If we substitute for λC_k a constant source S ($cm^{-3} s^{-1}$), we have an equilibrium concentration, ns of

$$ns = \frac{S}{15} \cdot \frac{a^2}{D}$$

(6)

We assume initially that S is half of the ionization flux. Now solving for the loss of argon by diffusion from a sphere with an equilibrium concentration, ns, we obtain a loss rate of 6/15 the incoming flux. Thus the true flux of neutrals to the atmosphere is the outgassing flux from the interior plus 3/15 of this flux, or a factor of 1.2 of the effusion rate from the interior. The rate of trapping of ^{40}Ar in the lunar rocks was estimated by Heymann and Yaniv (1970) to be 400 atoms $cm^{-2} s^{-1}$. If this represents half of the ion loss rate, then the ion loss rate is 800 $cm^{-2} s^{-1}$, consistent with the lower limit of the effusive flux estimated by Hodges and Hoffman (1974). In reality, only a fraction of the returning ions will be trapped in the grains, so these results are fully consistent.

Argon is lost from the atmosphere by photoionization and by electron impact ionization. At the Moon, the primary loss mechanism is photoionization. At Mercury, electron impact ionization is more important than at the Moon, but still less important than photoionization. The photoionization rate for argon at Earth orbit is given by Huebner *et al.* (1992) as 3.05×10^{-7} s^{-1} for quiet sun and 6.9×10^{-7} s^{-1} for active sun. This gives a lifetime against ionization at the Moon of 38 days for quiet sun, and 17 days for active sun. The value used to analyze the lunar ALSEP data was 18 days (Manka, 1973), but this is probably too short based on the mean monthly sunspot number at the time. For this analysis we will use an ionization lifetime for Ar at the Moon as 23 days, mid-way between quiet and active sun conditions. Adding an additional 14 days for nighttime, during which the argon is sequestered in the soil, the lifetime is 37 days. This is reasonably consistent with the lifetime derived by Hodges: 50 days. Using a time average, the effusion rate of new argon atoms is equal to the photoionization rate minus 6/15 of the rate of return of photoions to the surface. Thus the effusion rate is 80% of the photoionization rate if half of the photoions return to the surface as calculated by Manka and Michel (1971).

Assuming that the lifetime of argon in the lunar atmosphere is 37 days, 23 days for photoionization plus 14 days spent on the nightside, the average total column of ^{40}Ar would be 4.6×10^{9} cm^{-2}. The lunar average degassing rate required by the Apollo 17 lunar surface mass-spectrometer results with no recycling of ions is 2×10^{21} atoms s^{-1}.

The mean photorate at Mercury mean orbit is $2.94 \times 10^{-6}/2$, taking into account the time in darkness. Thus the lifetime of an argon atom in Mercury's atmosphere would be 7.9 days. Argon atoms diffusing into the atmosphere during nighttime would be subject to electron impact ionization, with a lifetime of about 89.7 days. On average the argon would persist in the atmosphere until rotated into the sunlight. The lifetime of argon in the lunar atmosphere is between 16.8 (active sun) and 38.6 days (quiet sun), plus 14 days in darkness. The lifetime of an argon atom in the lunar atmosphere during the ALSEP program was about 37 days. If the flux out of Mercury's crust is 1830 atoms cm^{-2} s^{-1} (Table 2) and the lifetime is 7.9 days, the average column abundance would be 1.3×10^{9} cm^{-2}, roughly comparable to the lunar column abundance.

CONCLUSIONS

We expect the atmospheric argon abundance at Mercury to be less than or comparable to that at the Moon. This is in sharp contrast with the sodium and potassium atmospheres of the two bodies, where the Mercurian abundance of sodium is two orders of magnitude greater than that at the Moon. This results from differences in the source processes of the alkalis and the rare gases. The former are probably preferentially derived from the surface by photon-stimulated desorption (Killen *et al.*, 2001; McGrath *et al.*, 1986), which

increases as the inverse square distance from the sun, although evaporation (Sprague, 1990), ion-sputtering (Potter and Morgan, 1990), and meteoritic vaporization (Cintala, 1992; Killen *et al*, 2001) also play important roles. The means of replenishing the surface with a fresh supply of alkalis has been debated in the literature. Whereas Sprague (1990) has argued that the alkalis are brought to the surface by diffusion, Killen and Morgan (1993 a, b) have argued that diffusion of the alkalis is inefficient, and that meteoritic gardening is sufficient. In contrast, the argon, being a noble gas, easily diffuses through a rock (e.g. Mussett, 1969), and readily evaporates at the surface (Hodges, 1975; 1977; Hodges *et al*., 1973).

Although the diffusion coefficients depend exponentially on temperature, the effusive flux is limited by the radiogenic production rate and by the distance between connected pore space. These parameters have been assumed to be fractal. At any given time after solidification, there will be a pulse of diffusant at the surface of a given size grain or unit. For a fractal distribution, then, at a given time a different size of grain or unit will be the major source of gas to the pore space. For two very different diffusion regimes a different size unit will dominate the source at a given time. If there size units are all available, the flux out of the crust will depend less on temperature (diffusion coefficient) and more on the distribution of unit sizes. Loss rates from the atmosphere are much larger at Mercury than at the Moon because photoionization loss dominates. Even though the ion recycling rate may be much larger at Mercury than at the Moon, this will not alter our results by more than a factor of two.

In future work, we will consider how the Mercurian magnetosphere affects the loss of argon. Because argon is both heavy and accommodated to the surface temperature, its scale height will be much smaller than the distance to the magnetopause. It is important to model this effect on the argon loss rate in order to understand measurements of atmospheric argon.

Appendix I.

The flux of argon diffusing out of the regolith at time, t, for $D=10^{-19}$ cm^2 s^{-1} is given by:

$$frac = \int_{1.25 \cdot 10^3}^{2.5 \cdot 10^6} \int_{1}^{300} \left[\left[(0.265) \cdot \left[1 + 1 \cdot \exp\left[-\left[\frac{\left(0.003 \cdot z^{0.8} \cdot a\right) - \mu}{\alpha} \right]^\gamma \right] \right] \cdot \left[\frac{(x0(z) \cdot a - \mu)}{\alpha} \right]^{\frac{\gamma}{2}} \right] - \frac{0.634}{1 + 0.003 \cdot z^{0.8} \cdot a} \right] \frac{(a)^{-2.5}}{0.666667} da \; dz$$

(A1.1)

for photoelectrons of energy 0.01<E<0.03 keV, and

$$F3(E) = -5.399 \cdot 10^{10} + -1.933 \cdot 10^{11} \cdot \exp(-E) + \frac{2.082 \cdot 10^{11}}{(1+E)} + \frac{\left[4.052(10)^{10}\right]}{\left(1+E^2\right)},$$

(A2.5)

for "cool" electrons of energy 0.03<E< 0.8 keV. The electron impact ionization rate was found by integrating

$$ni = \int_{0.015}^{0.03} 2\pi \cdot 0.001 \cdot F2(E)dE + \int_{0.03}^{0.8} 2\pi \cdot nar \cdot \sigma(E) \cdot F3(E)dE$$

(A2.6)

where the electron impact cross section is taken as a constant near threshold. The resulting loss rate for electron-impact ionization at Mercury is 1.29×10^{-7} N s^{-1}, where N is the argon column cm^{-2}.

Acknowledgements

REFERENCES

BINDER, A.B. (1980) Shallow Moonquakes: Argon release mechanism. *Geophys. Res. Lett.* 7, 1011-1013.

BRANDT, S. B. and E. N. BARTNITSKIY (1964) Losses of radiogenic argon in potassium-sodium feldspars on heat activation, *Int. Geol. Rev*, 6, 1483.

BROADFOOT, A.L., D.E. SHEMANSKY and S. KUMAR (1976) Mariner 10 - Mercury Atmosphere, *Geophys Res. Lett.* 3, 577-580.

CINTALA, M.J. (1992) Impact-induced thermal effects in the lunar and Mercurian regoliths. *J. Geophys. Res.* 97, 947-973.

FECHTIG, H., W. GENTNER, and J. ZAHRINGER (1960) Argonbestimmungen an Kalium-mineralien- VII. Diffusionrverluste von argon mineralien und ihre auswirkung aud die kalium-argon-alterbestimmung, *Geochim. Cosmochim. Acta* 19, 70.

assuming that the minimum radius at depth, z, is $r_0 = 0.003z^{0.8}$ cm, the size distribution at a given depth, z, is $f(r) = (r/r0)^{-2.5}$, n and the flux is 1.456×10^{-3} frac. The constants α, γ, and μ are given in Table A1. The constant, 1.45×10^{-3} is the total number of ^{40}K atoms per unit volume, assuming a density of 2.6 g cm^{-3}, and a lunar crustal K abundance of 300 ppm and the scale factor 10^{-18}, which was not included in frac for plotting purposes. The results can be scaled to the K abundance and the density.

Appendix II. The electron impact ionization rate at Mercury

In order to determine the electron impact loss rate at Mercury we fit the electron impact cross section, $\sigma(E)$, as a function of energy, E (keV), given by Rapp and Englander-Golden (1965) to a function, F(x). We integrated this function over the electron energy at Mercury given by Russell et al. (1988).

$$F1(E) = \begin{bmatrix} \exp[-(1+35 \cdot E)] \\ \dfrac{1}{(4 \cdot E)^3} \\ 1 + \exp[-(3.7 \cdot E)^2] \\ \cos(3.2E) \end{bmatrix} \tag{A2.1}$$

$$S = \begin{pmatrix} -9.676 \\ -4.416 \times 10^{-4} \\ 1.567 \\ 0.443 \end{pmatrix} \tag{A2.2}$$

The cross section is given by

$$\sigma(E) = -9.676\exp[-1+35 \cdot E)] + 0.433 \cdot \cos(3.2 \cdot E) + 1.567 \cdot \left[1 + \exp[-(3.7 \cdot E)^2]\right] + \frac{4.416 \cdot 10^{-4}}{(4 \cdot E)^3} \tag{A2.3}$$

where σ is in barns (the area of the hydrogen nucleus).

The electron flux (particles cm^{-2} s^{-1} ster^{-1} keV^{-1}) as a function of energy in keV (Russell et al.1988) is fit to

$$F2(E) = 9.17 \cdot 10^{13} + 1.73 \cdot 10^9 \cdot \left(1 + \frac{1}{E}\right) - \left[\frac{(9.184 \times 10^{13})}{\left[1 + \left(\frac{E}{2}\right)^2\right]}\right] \tag{A2.4}$$

HEIKEN, G.H., D.T. VANIMAN, and B.M. FRENCH (1991) *Lunar Sourcebook*, Cambridge Univ. Press, Cambridge, England.

HEYMANN, D. AND A. YANIV (1970) [40]Ar anomaly in lunar samples from Apollo 11, *Proc. Lunar Sci. Conf,* 1261 - 1267.

HODGES, K.V. (1991) Pressure-Temperature-Time Paths, *Ann. Rev. Earth Planet Sci. Lett.* **19**, 207-236.

HODGES, R.R., Jr. (1975) Formation of the lunar atmosphere, *The Moon* **14**, 139-157.

HODGES, R. R, Jr. (1977) Release of radiogenic gases from the Moon, *Physics of Earth and Planetary Science Interiors,* **14**, 282 - 288.

HODGES, R.R. (1980) Lunar cold traps and their influence on argon-40, *Proc. Lunar Planet. Sci. Conf. 11th,* 2463-2477.

HODGES, R.R., Jr., and J.H. HOFFMAN (1974) Episodic release of [40]Ar from the interior of the Moon, *Proc. Lunar Sci. Conf.* **5th,** In *Geochim. Cosmochimica Acta* **3,** 2955 - 2961.

HODGES, R.R., J.H. HOFFMAN, F.S. JOHNSON and D.E. EVANS (1973) Composition and dynamics of lunar atmosphere, *Proceedings of the Lunar Science Conf.,***4th,** In *Geochimica Cosmochimica Acta* **3** (Suppl. 4), 2855 - 2864.

HOFFMAN, J.H., R.R. HODGES, F.S. JOHNSON and D.E. EVANS (1973) Lunar atmospheric composition results from Apollo 17, *Proceedings of the* 4th *Lunar Science Conf.,* In *Geochimica Cosmochimica Acta* **3** (Suppl. 4), 2865 - 2875.

HUEBNER, W.F., J.J. KEADY, AND S.P. LYON (1992) Solar photo rates for planetary atmospheres and atmospheric pollutants, *Astrophys. Space Sci.,* **195,** 1 - 294.

KABIN, K., T.I. GOMBOSI, D.L. DEZEEUW, AND K.G. POWELL (2000) Interaction of Mercury with the solar wind, *Icarus* **143,** 397- 406.

KILLEN, R.M. AND T.H. MORGAN (1993) Diffusion of Na and K in the uppermost regolith of Mercury, *J. Geophys. Res.* **98,** 23589 - 23601.

KILLEN, R.M. AND T.H. MORGAN (1993) Maintaining the Na atmosphere of Mercury, *Icarus* **101,** 293 - 312.

LEE, J.K.W. AND A.A. ALDAMA (1992) Multipath diffusion: A general numerical model. *Computers in Geosciences,* **18,** 531-555.

LOVERA, O.M., F.M. RICHTER, T.M. HARRISON (1989) $^{40}Ar/^{39}Ar$ geothermometry for slowly cooled samples having a distribution of diffusion domain size, *J. Geophys. Res.* **94**, 17917 - 17936.

LUHMANN, J.G., C.T. RUSSELL, AND N.A. TSYGANENKO (1998) Disturbances in Mercury's magnetosphere: Are the Mariner 10 "substorms" simply driven?, *J. Geophys. Res.* **103**, 9113 - 9119.

MANKA, R.H. (1973) Plasma and potential at the lunar surface, In *Photon and Particle Interactions with Surfaces in Space*, Proceedings of the 6th ESLAB Symposium held in Noordwijk, Holland, Sept. 26-29, 1972, (ed. R. J. L. Grard), p. 347, D. Reidel, Dordrecht, Holland.

MANKA, R.H. AND F.C. MICHEL (1971) Lunar atmosphere as a source of lunar surface elements, *Proc.* 2nd *Lunar Science Conf.*, In *Geochimica Cosmochim Acta* **2** (Suppl. 2), 1717 - 1728.

MANKA, R.H. AND F.C. MICHEL (1973) Lunar Ion Flux and Energy, In *Photon and Particle Interactions with Surfaces in Space*, Proceedings of the 6th ESLAB Symposium held in Noordwijk, Holland, Sept. 26-29, 1972, (ed. R. J. L. Grard), pp. 429-442, D. Reidel, Dordrecht, Holland.

MCGRATH, M.A., R.E. JOHNSON, AND L.J. LANZEROTTI (1986) Sputtering of sodium on the planet Mercury. *Nature* **323**, 694-696.

METZGER, A.F., J.I. TROMBKA, R.C. REEDY AND J.R. ARNOLD (1974) Element concentrations from lunar orbital gamma ray measurements. *Proc.* 5th *Lunar Sci. Conf.* In *Geochim. Cosmochim. Acta.* **3** (Suppl. 5), 1067 - 1078.

MUSSETT, A.E. (1969) Diffusion measurements and potassium-argon method of dating, *Geophys. J. Roy. Astron. Soc.* **18**, 257 - 303.

NAKAMURA, Y., J. DORMAN, F. DUENNEBIER, M. EWING, D. LANMLEIN, AND G. LATHAM (1974) High frequency lunar teleseismic events, *Proc.* 5th *Lunar Sci. Conf.*, In *Geochim. Cosmochimica Acta* **3**, 2883- 2890.

POTTER, A.E. AND T.H. MORGAN (1990) Evidence for magnetospheric effects on the sodium atmosphere of Mercury. *Science* **248**, 835-838.

RAPP, D. AND P. ENGLANDER-GOLDEN (1965) Total cross sections for ionization and attachment in gases by electron impact. I. Positive Ionization, *Journ. Chem. Phys.* **43**, 1464 - 1479.

RUSSELL, C.T., D.N. BAKER, AND J.A. SLAVIN (1988) The Magnetosphere of Mercury, In *Mercury* (eds. F. Vilas, C. Chapman and M. S. Matthews) pp. 514 - 561. Univ. Arizona Press, Tucson, Arizona, USA.

SARANTOS, M. 2002. *A model for magnetosphere-exosphere interaction at Mercury*. Ph.D. Thesis, Rice University, Houston, Texas.

SARANTOS, M., P.H. REIFF, T.W. HILL, R.M. KILLEN, AND A.L. URQUHART (2001) A Bx-interconnected magnetosphere model for Mercury, *Planetary and Space Science* **49**, 1629 - 1635.

SHEMANSKY, D.E. (1988) Revised atmospheric species abundances at Mercury: The debacle of bad g values. *Mercury Messenger* **2**, 1.

SPRAGUE, A.L. (1990) A diffusion source for sodium and potassium in the atmospheres of Mercury and the moon. *Icarus* **84**, 93-105.

TAYLOR, S.R. AND P. JAKES (1974) The geochemical evolution of the Moon. *Proc. 5th Lunar Sci. Conf.*, In *Geochim. Cosmochimica Acta* **3**, 1287 - 1305.

TURCOTTE, D.L. AND G. SCHUBERT (1988) Tectonic implications of radiogenic noble gases in planetary atmospheres, *Icarus* **74**, 36 - 46.

TURCOTTE, D.L. (1997) *Fractals and chaos in geology and geophysics*, Cambridge Univ. Press, 221 pp.

WASSERBURG, G.J. (1954) ^{40}Ar -^{40}K Dating, In *Nuclear Geology* (ed. H. Faul), pp. 341-349, Wiley, New York, USA.
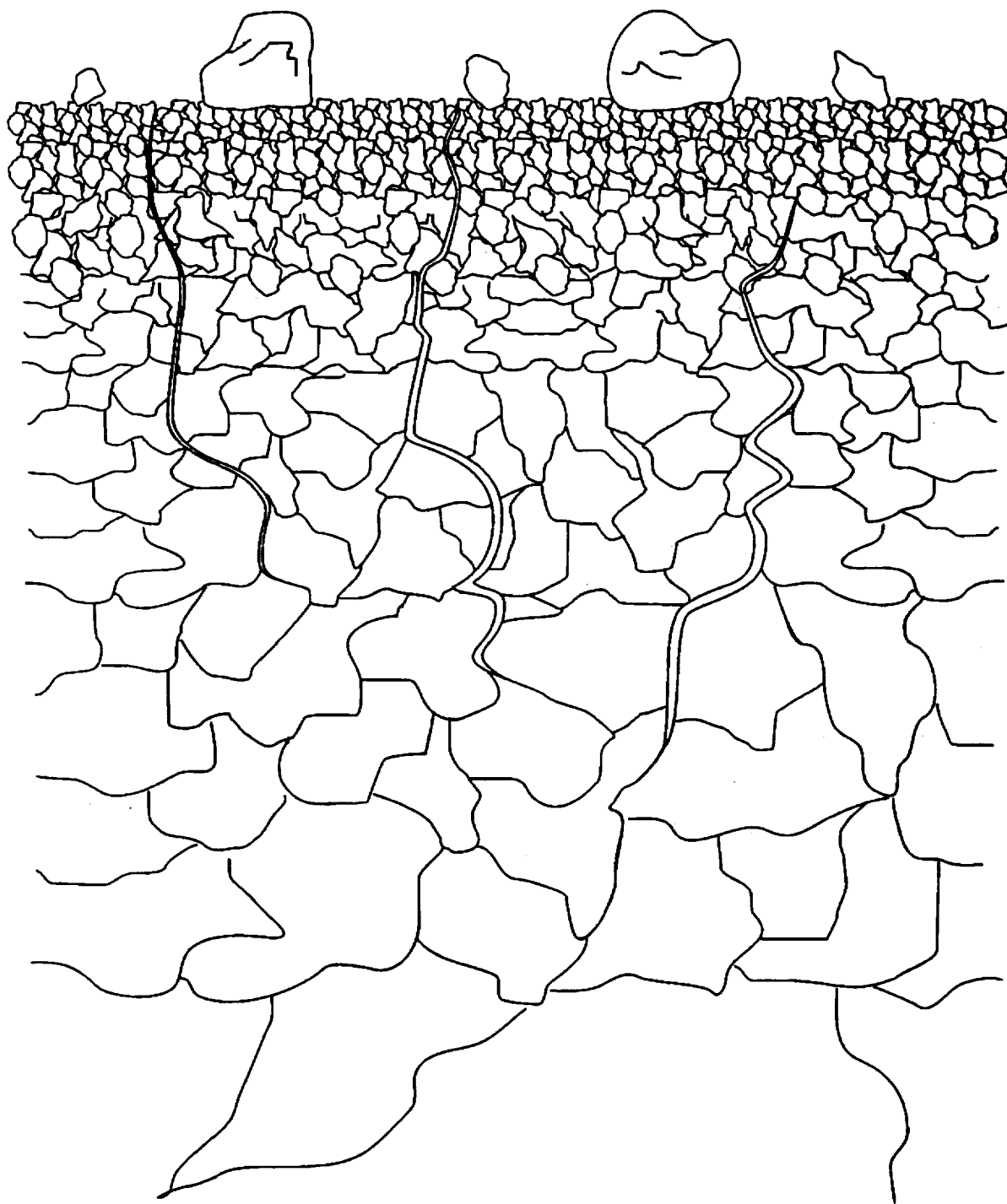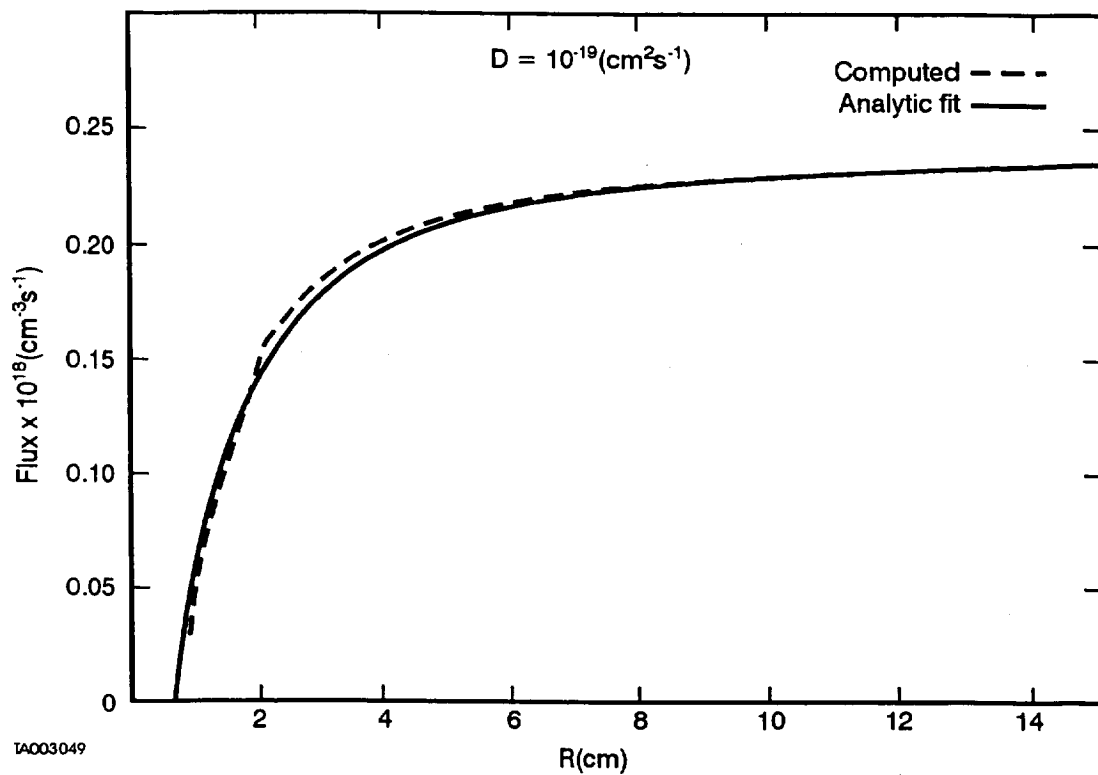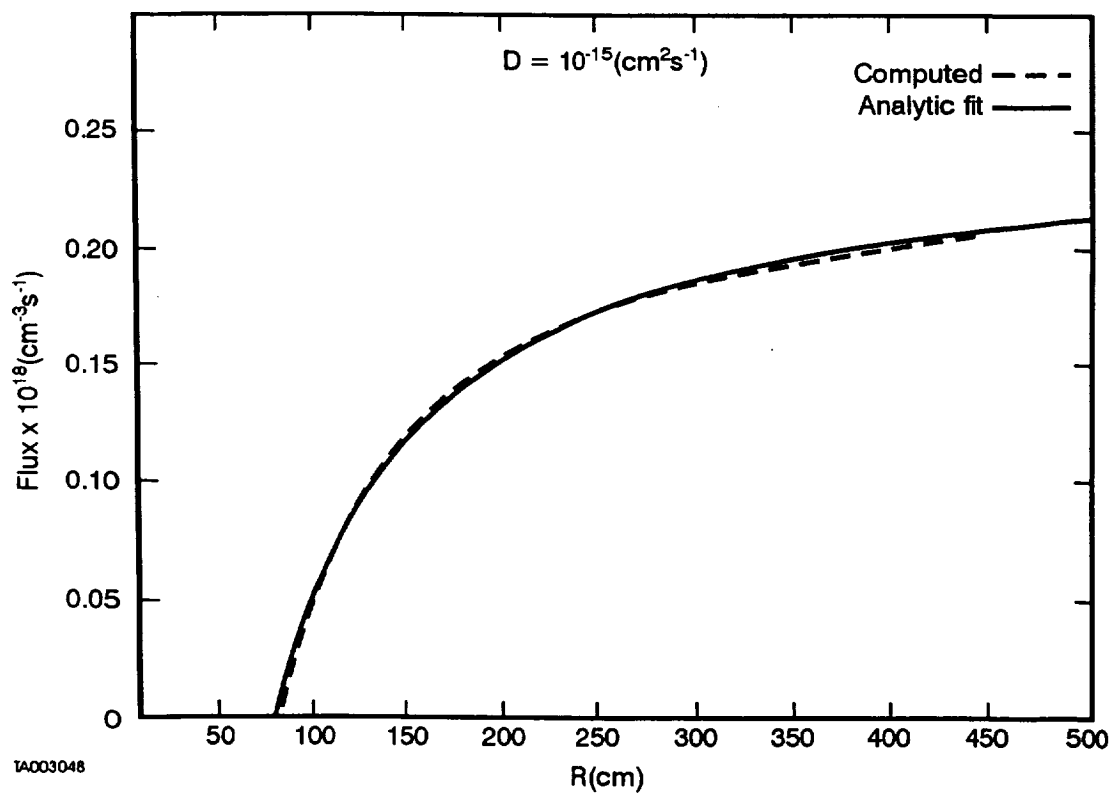
IA003210

Figure 1.

Figure 2.

Figure 3.

18

18

Table A1. Parameters for analytical fit to diffusive flux.

Log (D)	α	γ	μ
-15	15.0	1.0	0.001
-19	1.5	0.6	0.001
-24	0.11	0.52	0.001

Figure Captions

Figure 1. The distribution of effective rock sizes, illustrated here in cartoon form, is assumed to be fractal with a fractal dimension of 2.5. The smallest unit at the surface is 30 μm. The smallest unit size at depth, z, is 0.003 $z^{0.8}$ (cm), where z is in cm. Thus the smallest distance to a connected pore space at a depth of 25 km is 3.9 meters

.

Figure 2. Flux of argon atoms per unit volume from spheres of radius, R, at 3.1 g yr for diffusion coefficient, $D=10^{-19}$ cm^2 s^{-1}. This diffusion coefficient, measured for orthoclase at 275 K, is within the range of values appropriate for the lunar crust. The flux as computed with the multipath diffusion code is the dashed line, and the analytical fit to these results is the solid line. Without radiogenic production, the curve would resemble a Weibull distribution curve, with a maximum flux at a radius depending on diffusion coefficient and time. With radiogenic production, the curve becomes asymptotic at large radii because argon continues to be produced within the rock.

Figure 3. The same as Figure 1 for $D=10^{-15}$ cm^{-2} s^{-1}. This diffusion coefficient, measured for anorthite at 450 K, is assumed to be appropriate for the crust of Mercury.

Evidence for space weather at Mercury

R. M. Killen,[1] A. E. Potter,[2] P. Reiff,[3] M. Sarantos,[3]

B. V. Jackson,[4] P. Hick,[4] B. Giles[5]

Abstract. Mercury's sodium atmosphere is known to be highly variable both temporally and spatially. During a week-long period from November 13 to 20, 1997, the total sodium content of the Hermean atmosphere increased by a factor of 3, and the distribution varied daily. We demonstrate a mechanism whereby these rapid variations could be due to solar wind-magnetosphere interactions. We assume that photon-stimulated desorption and meteoritic vaporization are the active source processes on the first (quietest) day of our observations. Increased ion sputtering results whenever the magnetosphere opens in response to a southward interplanetary magnetic field (IMF) or unusually large solar wind dynamic pressure. The solar wind dynamic pressure at Mercury as inferred by heliospheric radial tomography increased by a factor of 20 during this week, while the solar EUV flux measured by the Solar EUV Monitor (SEM) instrument on board the Solar and Heliospheric Observatory (SOHO) increased by 20%. While impact vaporization provides roughly 25% of the source, it is uniformly distributed and varies very little during the week. The variations seen in our data are not related to Caloris basin, which remained in the field of view during the entire week of observations. We conclude that increased ion sputtering resulting from ions entering the cusp regions is the probable mechanism leading to large rapid increases in the sodium content of the exosphere. While both the magnitude and distribution of the observed sodium can be reproduced by our model, in situ measurements of the solar wind density and velocity, the magnitude and direction of the interplanetary magnetic field, and Mercury's magnetic moments are required to confirm the results.

1. Introduction

Six elements have been observed in the Hermean exosphere: H, He, O, Na, K, and Ca. The first three were observed with the ultraviolet spectrometer (UVS) on board the Mariner 10 spacecraft [*Broadfoot et al.*, 1976], while the last three were discovered via ground based observations [*Potter* and *Morgan*, 1985, 1986; *Bida et al.*, 2000]. Only the sodium exosphere has been monitored over long timescales via its strong resonance transitions in the visible region: the D lines at 5889.95 and 5895.92 A. Mercury's sodium exosphere is characterized by rapid changes [on timescales less than a day], with high-latitude and midlatitude enhancements common [*Potter and Morgan*, 1990; 1997; *Potter et al.*, 1999]. These variations have been attributed to magnetosphere-solar wind interaction [*Potter and Morgan*, 1990] or to variations in the underlying terrain [e.g., *Sprague et al.*, 1998].

[1]Instrumentation and Space Research, Southwest Research Institute, San Antonio, Texas.

[2]National Solar Observatory, Tucson, Arizona.

[3]Department of Space Physics and Astronomy, Rice University, Houston, Texas.

[4]Center for Astrophysics and Space Sciences, University of California, San Diego, La Jolla, California.

[5]NASA Goddard Space Flight Center, Interplanetary Physics Branch, Greenbelt, Maryland.

In November 1997 a week-long series of data was obtained with the McMath-Pierce solar telescope at Kitt Peak, Arizona [*Potter et al.*, 1999]. Images of the extended sodium nebula about Mercury were produced from three-dimensional spectra obtained at a spatial resolution of 1.0x0.5 arc sec (") with the 10"x10" Richardson image slicer [*Richardson et al.*, 1984] on the McMath-Pierce solar telescope at Kitt Peak, Arizona. The data were absolutely calibrated in sodium D₂ emission (Appendix A) and then to column abundance of Na around the planet (Appendix B). During the week of November 13-20, 1997, the total atmospheric sodium inventory on the Sunlit side of the planet increased by a factor of 3. Details of the data and their reduction are given in section 2.

Since Mercury's sodium exosphere was discovered [*Potter and Morgan*, 1985] the relative importance of various proposed source processes has been widely discussed in the literature. Photon-stimulated desorption was the first mechanism proposed as the major source of the Mercurian atmosphere [*McGrath et al.*, 1986] and was later considered by *Cheng et al.* [1987], *Morgan and Shemansky* [1991], and *Shemansky and Morgan* [1991]. The distribution of Na at the Moon, which peaks at the subsolar point, [*Flynn and Mendillo*, 1995], and at times at Mercury [*Killen et al.*, 1990], as well as the sodium line profiles [*Killen et al.*, 1999; *Stern et al.*, 2000] are consistent with this source process. *Madey et al.* [1998] measured photon stimulated desorption (PSD) yields and concluded that PSD can account for the measured abundances. Although thermal desorption certainly occurs it is not considered here because it is a secondary process acting on adsorbed atoms. *Morgan et al.* [1988] and *Cintala* [1992] concluded that, within the upper limits, impact vaporization can supply the sodium exosphere if photoions are efficiently

recycled; however, *Smyth and Marconi* [1995a] rejected an impact-vaporization source on the basis that such a model is inconsistent with the dynamic range of the data. Impact vaporization has gained increased interest following recent reports that the lunar exospheric density increased following meteor shower events, particularly the Leonids [*Smith et al.*, 1999; *Wilson et al.*, 1999; *Verani et al.* 1998; *Hunten et al.* 1991, 1998].

For a constant magnetosphere and solar wind, the production of sodium by all three processes, and loss by both photoionization and radiation-pressure-driven acceleration to escape velocity, should vary about the orbit from perihelion to aphelion in a smooth and predictable way [*Smyth and Marconi*, 1995a; *Smyth*, 1986; *Ip*, 1986, 1990].

The observed atmosphere does not follow the smooth behavior predicted by *Smyth and Marconi* [1995a,1995b] for either impact vaporization or for photon-stimulated desorption. Thus an additional process must be operating. Two competing mechanisms have been proposed for the origin of the short-term variability in Mercury's sodium and potassium exospheres [e.g., *Potter and Morgan*, 1990, 1997]: that they are associated with surface features [*Sprague et al.*, 1990, 1998] and that they are caused by solar wind-magnetosphere interactions with resultant time-variable ion sputtering [*Potter and Morgan*, 1985; *Killen et al.*, 1990; *Potter and Morgan*, 1990; *Potter et al.*, 1999]. In contrast to the Moon, whose surface is directly exposed to the solar wind except when the Moon is inside the Earth's magnetosphere [e.g., *Mendillo et al.*, 1999; *Potter et al.*, 2000], the solar wind at Mercury is deflected by Mercury's magnetic field. However, the solar wind can directly impinge on the surface when the magnetopause is pushed to the surface by an unusually high solar wind pressure [*Goldstein et al.*, 1981; *Kabin et al.*, 2000], or through the cusps where field lines are open [*Luhmann et al.*, 1998; *Sarantos*, 2000]. Because of Mercury's weak magnetic field, ion sputtering following magnetospheric storms or substorms should also occur in wide auroral bands which may extend to the dayside [*Ip*, 1987].

Solar wind-magnetospheric effects at Mercury have been suggested on the basis of rapidly varying enhancements in the Na column abundance, seen principally [but not exclusively] at high latitudes [e.g., *Killen et al.*, 1990; *Potter and Morgan*, 1990, 1997]. Enhancements in sodium abundance are most often seen at high southern latitudes, but they also occur at high northern latitudes, and at midlatitudes. Charged particle sputtering has been proposed as the cause of these rapid changes [*Potter* and *Morgan*, 1990; *Potter et al.*, 1999], but has never been quantitatively estimated. *Goldstein et al.* [1981] and *Cheng et al.* [1987] estimated the production of H and He by ion sputtering by scaling observations of polar cap fluxes in the Earth's auroral regions, and *Ip* [1987] estimated the size of the auroral zones at Mercury by trajectory analysis. Precipitation onto the auroral zones was estimated by *Baker et al.* [1987] using a scaled Earth magnetosphere model. Expected variations in the total abundance of sodium and its spatial distribution about Mercury and the Moon have been modeled previously for mono-energetic source atoms *with* various spatial distributions [*Smyth and Marconi*, 1995a, 1995b]. However, there has never been a study in which variations seen in a particular data set have been modeled including the effect of solar wind-magnetosphere interactions. Because Mercury's magnetic field is weak [400 nT at the surface] and the solar wind is strong, the size of the polar cusps is expected to vary radically at Mercury [*Sarantos*, 2000]. Mercury's auroral zones are expected to be large [*Ip*, 1987], but are not considered herein as a source for dayside enhancements.

We consider meteoritic vaporization, photon-stimulated desorption, and ion sputtering as the three principal sources of atmospheric sodium (Plate 1). We do not consider thermal desorption because it is a secondary source process acting on physically adsorbed atoms, not chemisorbed or bound atoms. We assume that solar wind ions directly penetrate to the surface along open field lines. The solar wind density and velocity at Mercury, required as input to both the magnetosphere model and source code, were obtained from a three-dimensional reconstruction of interplanetary scintillation (IPS) data [e.g., *Jackson et al.*, 1997a, 1997b, 1998]. The interplanetary magnetic field (IMF) is an important parameter in determining the morphology of the magnetosphere and, consequently, the loci of open field lines. Because the exact magnitude and orientation of the interplanetary magnetic field is unknown at the position of Mercury for the times of our observations, we assumed various regions of open field lines and show that this is consistent with the magnetosphere model for various values of IMF. Loss is by photoionization or migration to the nightside. Adsorption on the surface is not considered a loss process, since such adsorbed atoms will thermally desorb and be reemitted to the atmosphere.

The impact vaporization is calculated following the planar impact approximation [*Melosh*, 1989; *Morgan* and *Killen*, 1998]. Sodium in the meteorites is assumed to be completely vaporized. Photosputter rates were scaled from laboratory measurements [*Yakshinskiy* and *Madey*, 1999] to match our quiet time observation, November 13, 1997. Details of the model are given in section 3.

2. Observations and Data Reduction

An excellent week-long record of Mercury's sodium atmosphere was obtained from November 13 to 20, 1997, excluding November 17 and 19, using the stellar spectrograph at the McMath-Pierce solar telescope on Kitt Peak, Arizona. Details of the observations are given in Table 1. These observations are obtained during daylight using a Richardson image slicer [*Richardson et al.*, 1984; *Pierce*, 1965]. The image slicer divides a 10"x10" area of sky into 10 slices which are stacked vertically into the entrance slit of the echelle spectrograph. The resulting pixel size is 1"x0.5", but each pixel was divided into two 0.5" square pixels for modeling. The echelle spectrograph was set to provide spectra of Mercury covering 15 A centered on ~5890 A so that both D lines are obtained. The data are in the form of an image cube with two spatial dimensions and one wavelength dimension. A spectrum, obtained at a spectral dispersion of 20 mA, is shown in Figure 1.

From each spectrum the total Na D_2 emission from the atmosphere was extracted. The three-dimensional data set was reduced in a self-consistent manner using software developed by *Potter et al.* [1999]. Considerable effort is involved in the reduction of these spectral images to column abundance maps. Details of the data reduction technique are given by *Potter et al.* [1999], and briefly outlined in Appendix A. The spectra are calibrated to absolute intensity by comparison of
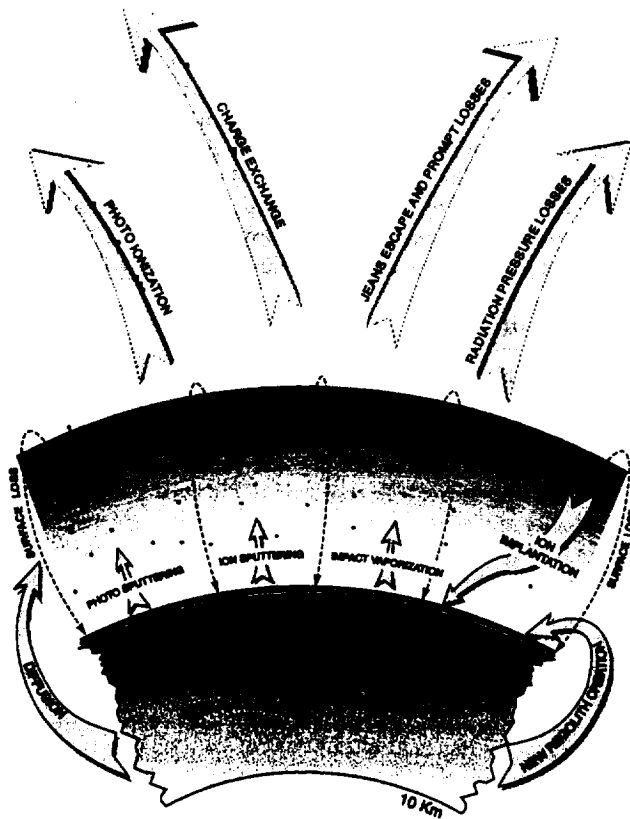
Plate 1. The expected source and loss processes for Mercury's exosphere are illustrated here. We do not consider diffusion from the interior or regolith gardening in our model because their timescales are much longer than the timescale of our observations. Our loss processes include photoionization and migration toward the terminator.
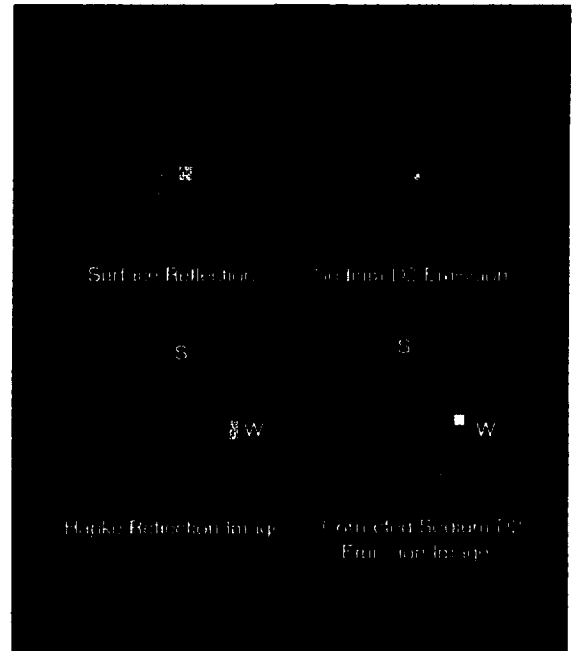

Plate 2. The three-dimensional data cubes are reduced to two-dimensional images by extracting the continuum intensity [left panel] and the sodium emission from the atmosphere [right panel] at each pixel. The continuum image varies smoothly from the subsolar point, whereas the atmospheric emission is irregular with rapid temporal variations. The images in the top panel have not been corrected for atmospheric smearing, while those on the lower panel are corrected. South is to the top, and west is to the right as seen in the telescope.

the continuum intensity over the disk of the planet with the Hapke bidirectional reflectance function at the appropriate wavelength and observation geometry [Hapke et al., 1975; Hapke, 1984; Domingue et al., 1997] using the known angular size of Mercury at the time of the observation. Given the known angular diameter of the disk we have used a Space Telescope Science Data Analysis System (STSDAS) Fourier deconvolution algorithm along with the Image Reduction and Analysis Facility (IRAF) package to deconvolve the signal and the atmospheric smearing (Plate 2). The deconvolution is accomplished by dividing the Fourier transform of the observed image by the Fourier transform of the theoretical image. Images of the calibrated sodium emission are shown in Plate 3 for each day.

After the images are calibrated to intensity, we use a radiative transfer program updated from that written by Killen [1988], to derive column abundance (Appendix B). The radiative transfer program is run pixel by pixel on a 0.5"x0.5" grid and iterates until the error (difference between measured and computed intensity) is minimal. Both the total abundance and distribution of sodium vary daily. Details of Mercury's ephemerides and observational parameters required for the data reduction are given in Table 1. The subobserver longitude is given at 1000 local time. (Most observations were obtained in the morning owing to the excellent morning seeing conditions at Kitt Peak.)

The zenith column density is near unity, ensuring that the line of sight column density near the limb is optically thick. During this week the total sodium content of the atmosphere increased by more than a factor of 3. The images reduced to column abundance are shown in Plate 4. The sodium initially

Table 1. November 1997 Data and Observational Parameters[a]

Date	$\Delta\lambda$, mA	PA,deg	Rm, AU	Dia"	γ (D1)	γ (D2)	λ (SS)	λ (SE)	f, deg
Nov. 13	112	40.5	0.44785	5.22	0.2925	0.2355	128.35	169.94	213
Nov. 14	120	42.1	0.44455	5.28	0.3259	0.2870	131.47	174.66	216
Nov. 15	128	43.7	0.44100	5.33	0.3579	0.2904	134.47	179.38	219
Nov. 16	136	45.3	0.44785	5.39	0.3844	0.3107	137.58	184.12	222
Nov. 18	151	48.9	0.42892	5.53	0.4345	0.3548	143.47	193.65	225
Nov. 20	165	52.7	0.41977	5.68	0.4648	0.3872	149.09	203.24	239

[a]$\Delta\lambda$, Doppler shift at Mercury relative to the Sun; PA, position angle; Rm, orbital distance; Dia", equatorial angular diameter in arc seconds γ, residual solar flux in the line at the Doppler shift of Mercury relative to the Sun; λ (SE) subobserver longitude at 10 AM local time; Subsolar λ (SS), Mercury subsolar longitude (east) at 1000 local time; f, true anomaly angle in degrees.
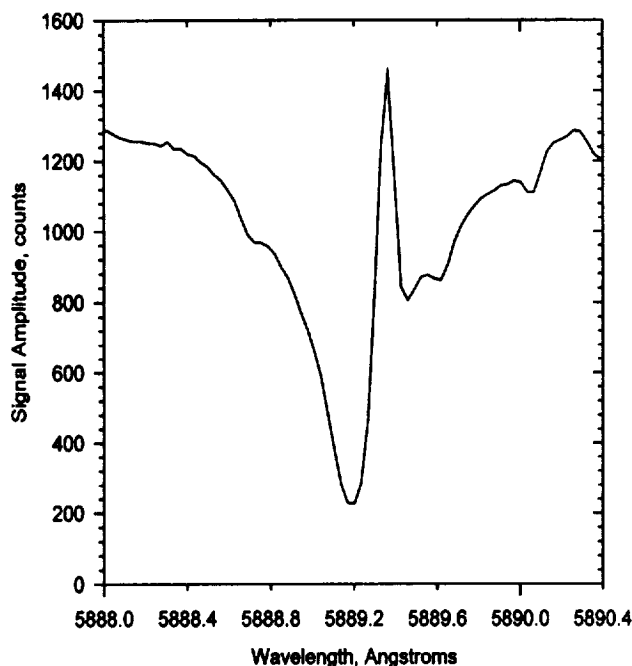
Figure 1. A spectrum such as that shown here is obtained at a spectral dispersion of 20 mA and a spatial resolution of 0.5x1.0 arc sec at each pixel of each 10"x10" observation. The Na D_2 emission from Mercury's atmosphere is Doppler shifted from the core of the solar Fraunhofer line by an amount depending on the radial velocity of Mercury with respect to the Sun. The spectra are reduced to intensity by calibrating the continuum emission with the Hapke formula for the bidirectional surface reflectance and scaling the counts to the known continuum emission [*Potter et al.*, 1999].

showed small enhanced emission near the poles, but as the week progressed the sodium content increased globally, becoming smoother and peaked at the subsolar point. The total sodium content on the Sunlit hemisphere is plotted versus time in Figure 2. Note that these column abundances are slightly smaller than those published in *Potter et al.* [1999] owing to improved calibration and radiative transfer.

3. Source Rates for the Neutral Atmosphere

We have modeled the following source processes: charged particle sputtering, impact vaporization, and photon-stimulated desorption. The source and loss processes are illustrated in cartoon form (Figure 1). The sodium line profiles indicate that the primary source mechanism must produce hot sodium (>1100 K at the equator) [*Killen et al.*, 1999]. This is consistent with all of the three mechanisms considered herein: ion sputter, photosputter, and meteoritic vaporization. It is inconsistent with thermal vaporization, which is not considered as a primary source process. Diffusion from the interior is also not considered herein because the timescale is too long to be of interest [*Morgan and Killen*, 1994].

We assumed a sodium composition for the regolith slightly enhanced over lunar (f_{Na}=0.0053). In order to test the theory that Caloris basin is the source of the time-variable sodium enhancements [*Sprague et al.*, 1990, 1998], we assumed a twofold enhancement of crustal sodium abundance inside the main ring of the Caloris basin with a radius of 670 km [*Pike*,

1988], centered at 195° longitude, 30°N. The Caloris basin region is modeled to be that region between 15° and 45°N latitude and 195° ± 15° longitude. Caloris basin was in the field of view partially under the sub-earth longitude during the entire observing run. Its position in the field of view is shown on the first (November 13) and last (November 20) days of our observations in Figure 3. The observation parameters for each day of observations are listed in Table 1. Additional parameters used in modeling are given in Table 2.

3.1. Ion Sputtering

We consider here the effect of direct penetration of ions through the cusps. The surface is assumed to be exposed to ion bombardment only where open flux tubes intersect the surface. The ion flux to the dayside surface is expected to vary as the magnetosphere responds to the solar wind density and velocity and the orientation of the interplanetary magnetic field [e.g., *Luhmann et al.*, 1998; *Sarantos*, 2000; *Kabin et al.*, 2000]. In order to quantitatively compute the ion sputter yield at Mercury we need to compute the size of the region on Mercury's surface that is directly accessible to solar wind ions (the cusp), and we need to estimate the solar wind flux to the surface.

Whether the interplanetary magnetic field (IMF) connects to the planetary magnetic field has been of great interest since the early days of magnetospheric research. In a closed magnetosphere, IMF field lines embedded in the solar wind plasma do not cross the planetary magnetopause. For scale lengths larger than the ion gyroradii, plasma on a given field line will not mix with neighboring plasma and must remain on
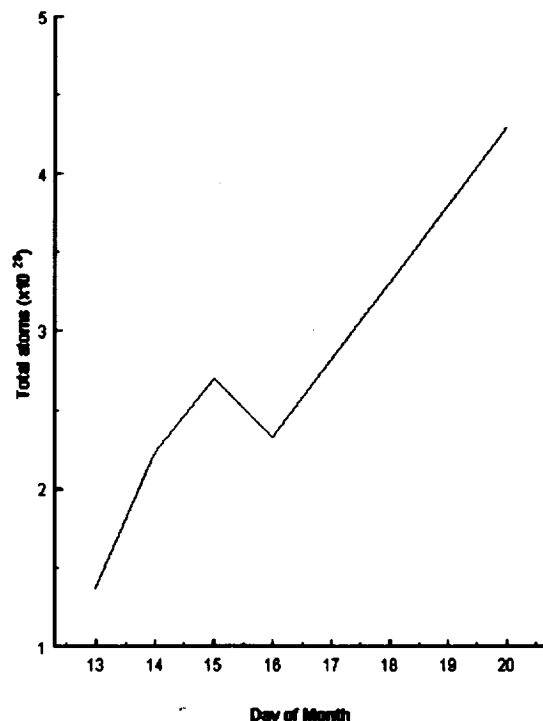

Figure 2. The total sodium content of the exosphere is plotted versus day of observation for the days November 13-20, 1997. Note that these estimates are lower than those given by *Potter et al.* [1999].
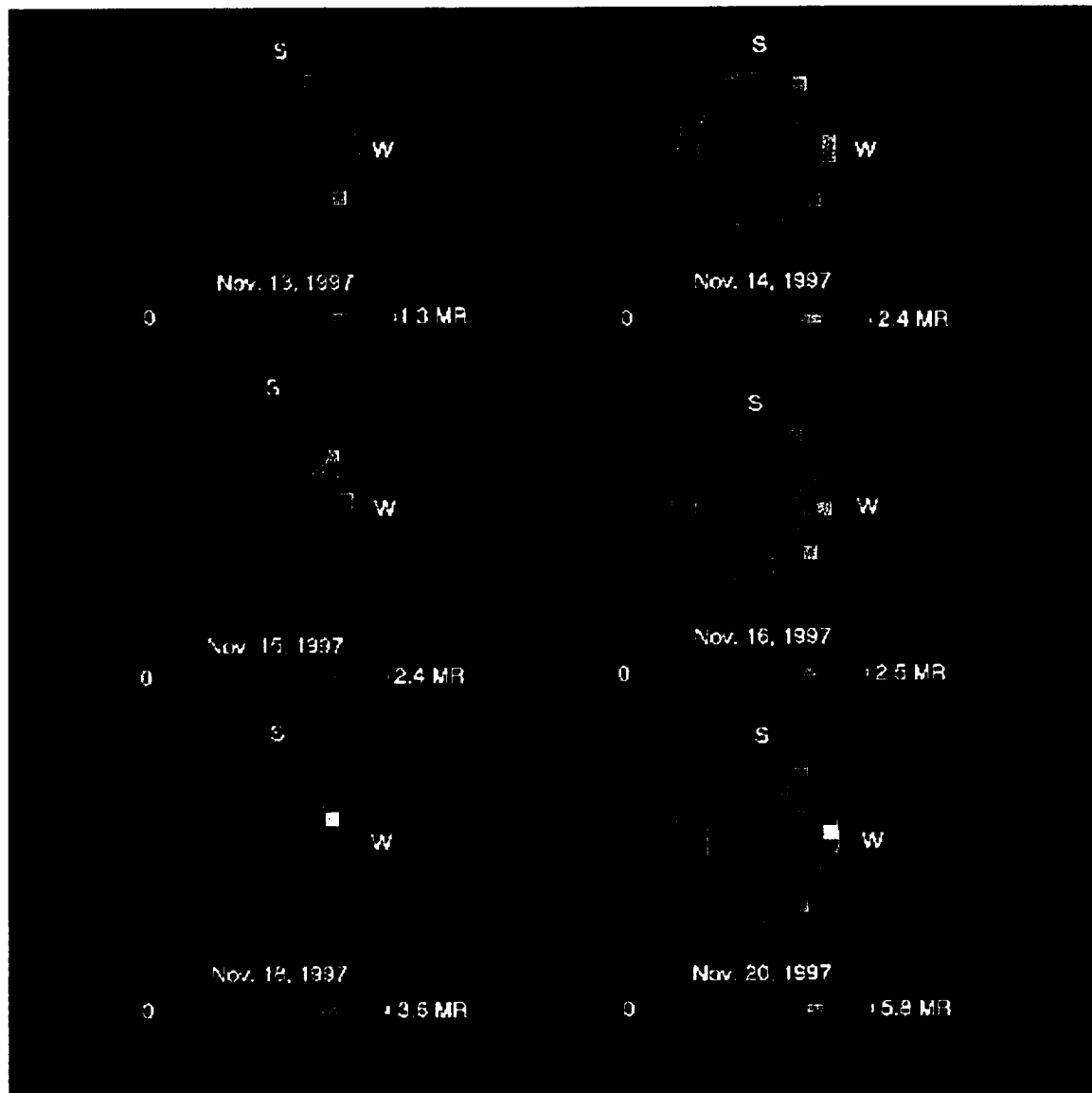
Plate 3. Absolutely calibrated images of Mercury's sodium D_2 emission in kR observed November 13-20, inclusive except for November 17 and 19, are illustrated here after deconvolution for atmospheric smearing using the Space Telescope Science Data Analysis (STSDAS) Fourier deconvolution algorithm and the IRAF package. The algorithm may overcorrect to make the images appear more patchy than they should be. The subsolar point is marked with a red dot.
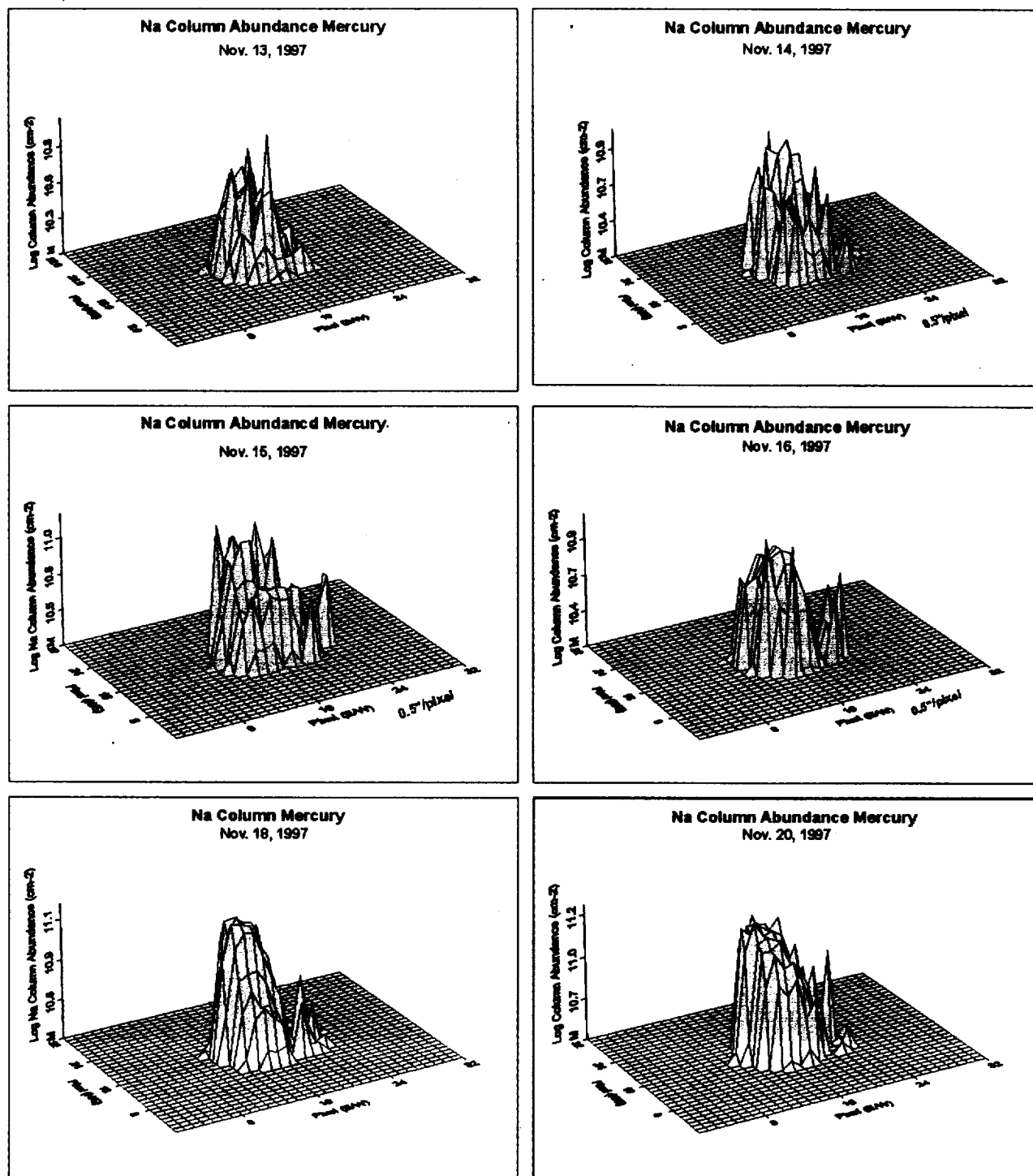
Plate 4. The images shown in Figure 1 are reduced to column abundance at each 1/2" pixel. The original 1"x0.5" pixels were divided in two to facilitate modeling. The total abundance grew by a factor of 3, while localized enhancements moved from north to south in this 1 week time frame. Enhancements in the southern hemisphere predominate. These images are reversed east-west from the observations in Plate 2, with the Sun to the left, but south is to the top. The easternmost pixels represent atmosphere that is illuminated beyond the shadow height. The unilluminated portion of the disk shows no column abundance, but the value is unknown.
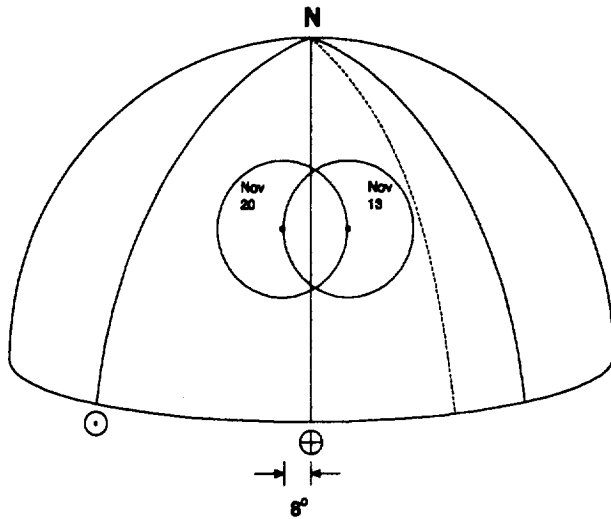
Figure 3. The position of the main ring of Caloris basin is illustrated relative to the sub-earth and subsolar longitudes on November 13 and 20, 1997. Caloris basin was rotating toward the subsolar longitude during this week. Caloris is centered at 30°N latitude and is 31° wide to the main ring [*Pike*, 1988].

the field line on which it originated. This is the well-known "frozen in flux" theorem. In such a scenario, there is no interconnection between the IMF and the magnetospheric field lines. However, it is known that solar wind plasma does penetrate into the terrestrial magnetosphere. In addition, because Mercury's magnetic field is so weak, the ion gyroradii can become larger than the planetary radius. We postulate that Mercury's magnetosphere has an open structure, meaning that Hermean field lines merge with interplanetary field lines, producing regions on the surface which are open to penetration by the solar wind.

We show how Mercury's magnetospheric configuration can respond to changes in the solar wind dynamic pressure and the interplanetary magnetic field (IMF) using a Toffoletto-Hill magnetosphere model modified for Mercury's dipole moment and location [*Toffoletto* and *Hill*, 1993; *Sarantos*, 2000].

The only spacecraft to have visited Mercury flew by the planet on March 29, 1974, September 21, 1974, and March 16, 1975. The locations of the bow shock and magnetosphere crossings were used to estimate a dipole moment $7x10^{-4}$ times that of the Earth. In addition to having a much smaller magnetic field, Mercury is embedded in a much stronger solar wind, with a density which scales roughly with distance R from the Sun as R^{-2} and a velocity which scales roughly as R^0. Pressure balance at the Earth demands

$$\frac{1}{2}\rho_E v_E^2 = \frac{1}{2\mu_0}B_E^2 = \frac{1}{2\mu_0}\frac{\mu_E^2}{R_{magE}^6} . \tag{1}$$

Similarly, at Mercury,

$$\frac{1}{2}\rho_M v_M^2 = \frac{1}{2\mu_0}B_M^2 = \frac{1}{2\mu_0}\frac{\mu_M^2}{R_{magM}^6} , \tag{2}$$

where ρ_E, v_E, and ρ_M, v_M are the solar wind density and velocity at Earth and Mercury, respectively. The constant μ_0 is the magnetic permeability of free space, and R_{ES} and R_{MS} are the corresponding orbital distances from the Sun of Earth

and Mercury, respectively. B_E and B_M are the strengths of the planetary magnetic fields of Earth and Mercury, respectively. The dipole moment of Mercury is only $7x10^{-4}$ that of the Earth. Given that the solar wind velocity scales as R^0 with distance from the Sun and solar wind density scales as R^{-2} and by means of comparison of (1) and (2),

$$\frac{R_{magM}}{R_{magE}} = \sqrt[3]{(\frac{R_{MS}}{R_{ES}}\frac{\mu_M}{\mu_E})} . \tag{3}$$

This would imply that the fractional size of Mercury's magnetosphere is 6% that of the Earth at perihelion and 7% at aphelion. We cannot simply scale the Earth magnetosphere to conditions at Mercury because Mercury is devoid of an ionosphere. However, a partially conducting surface at Mercury could play the role of a dynamically significant ionosphere. The lack of an ionosphere at Mercury allows an opportunity for studying how solar wind particles enter a magnetosphere and are precipitated onto the surface.

The TH93 model is a steady state open magnetosphere model. In the TH93 model the shape of the magnetopause consists of a hemisphere on the dayside attached to a semi-infinite cylinder on the nightside. The model solves the Laplace equation analytically. The internal field is based on *Voigt's* [1981] closed, three-dimensional model. The elongation of the tail is produced by stretching the dipole field by multiplying the two field components perpendicular to the tail by a parameter alpha. The penetration of the IMF into the magnetosphere is controlled by the distribution of the magnetic normal component at the magnetopause, as described by *Toffoletto* [1987] and *Toffoletto and Hill* [1993].

In brief, the open configuration of the magnetosphere is produced in the model by the so-called "interconnection" field which is added as a perturbation to the closed magnetic field. The extent of the open field lines depends critically on the degree of penetration of IMF B_x allowed in the model. The overall configuration of the magnetosphere depends on the shielding of the planetary magnetic dipole. For 60% penetration, cases with $B_z=5$ nT exhibited no open field lines for $B_x < 15$ nT; however, for the $B_z=0$ nT and all negative B_z, there are open field lines even in cases where only 20% penetration was allowed. The extent of open field lines is reduced as the percent penetration is reduced. We assumed a 25% penetration of the IMF in the models presented.

This model requires as input the solar wind density and velocity and the magnitude and direction of the interplanetary magnetic field (IMF). We assume that the solar wind impinging onto the surface through open field lines is responsible for the ion sputtering on the dayside. An important advance in solar terrestrial physics allows us to determine the solar wind flux at Mercury. We obtain solar wind density and velocity at the orbit of Mercury at the time

Table 2. Parameters Used in Calculations

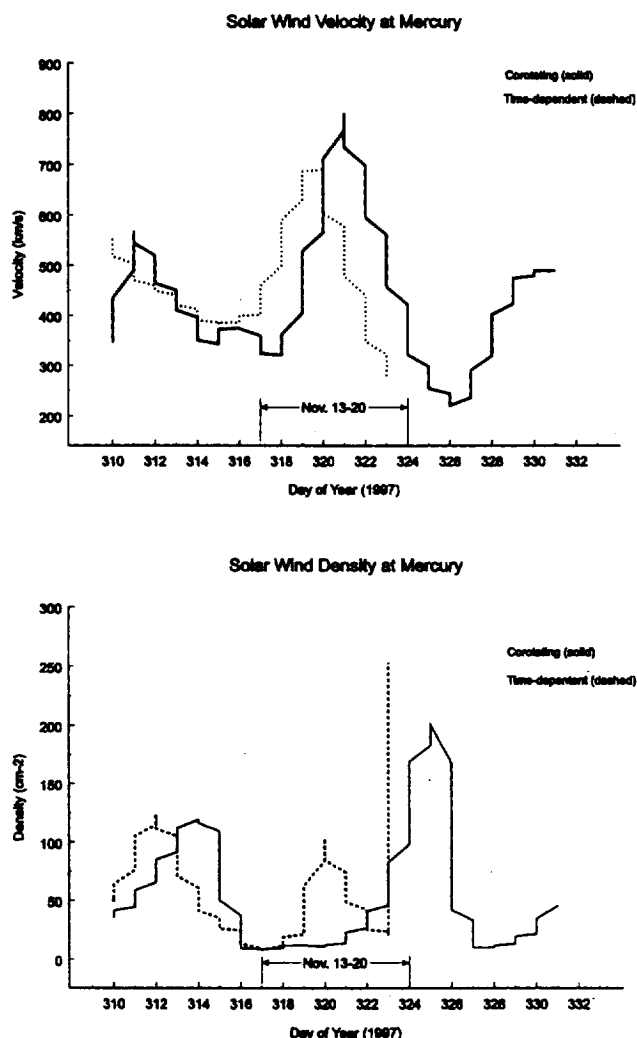| Parameter	Value
UV solar flux capable of PSD	$Ax10^{14}/R_{orb}^2$
Qphot	$1.14x10^{-21}$/photon
Qsolar wind	0.15
Regolith surface density	$7.5x10^{14}$ atoms cm^{-2}
f(Na)	0.0053
Photoionization lifetime	$6.255x10^4 R_{orb}^2$

Plate 5. (a) The solar wind velocity at Mercury as estimated by radial tomography of the interplanetary radio scintillation. Results of the corotating model [solid] and time-dependent model (dashed) are shown. (b) Solar wind density at Mercury estimated from corotating and time-dependent radial tomography of interplanetary scintillation (IPS) data. The dates of our observations are marked from November 13 (DOY 317) to November 20 (DOY 324). The corotating model is consistent with a steady increase in solar wind dynamic pressure during our observing run, but the increase in solar wind density on November 15, with a subsequent decline followed by a large increase on November 20, seen in the time-dependent model may be consistent with the increase in exospheric density seen on November 15. On the other hand, it may be spurious.

of our observations via a three-dimensional reconstruction of interplanetary scintillation [IPS] data [*Hick and Jackson*, 1994; *Jackson et al.*, 1997a, 1997b, 1998; *Asai et al.*, 1998]. IPS observations are obtained from the Solar Terrestrial Environment Laboratory (STELab), Japan, scintillation arrays observing radio sources at 0.91 m (327 MHz). The scintillation level is related to the integral of small-scale density variations along the line of sight extrapolated to 1 AU and fit to density monitored by spacecraft near Earth. The solar wind velocity and density inferred at Mercury at the times of our observations are shown in Plates 5a and 5b, respectively, and listed in Table 3 for the corotating model. Two different methods were used to estimate the solar wind

Table 3. Solar Wind at Mercury: Corotating Tomography for CR1929

Day	Density, cm^{-3}	Velocity, $km\ s^{-1}$	$\rho v\ x\ 10^8$ $cm^{-2}\ s^{-1}$
Nov. 13	8.8	324	2.85
Nov. 14	11.5	362	4.16
Nov. 15	11.8	529	6.24
Nov. 16	12.5	712	8.9
Nov. 17	22.9	735	16.8
Nov. 18	41.2	596	24.6
Nov. 19	83.1	457	38.0
Nov. 20	168.9	322	54.3

density and velocity at Mercury during our observations. The corotating method assumes that the solar wind source corotates with the Sun, and the time-dependent method has no such restriction. The two methods give generally similar results but have a slight temporal offset. Thus we cannot be confident of the timing of the solar wind impact at Mercury. We used the corotating results. Note, however, that the time-dependent model gives a peak in solar wind dynamic pressure on November 16, while the corotating model gives a peak on November 20.
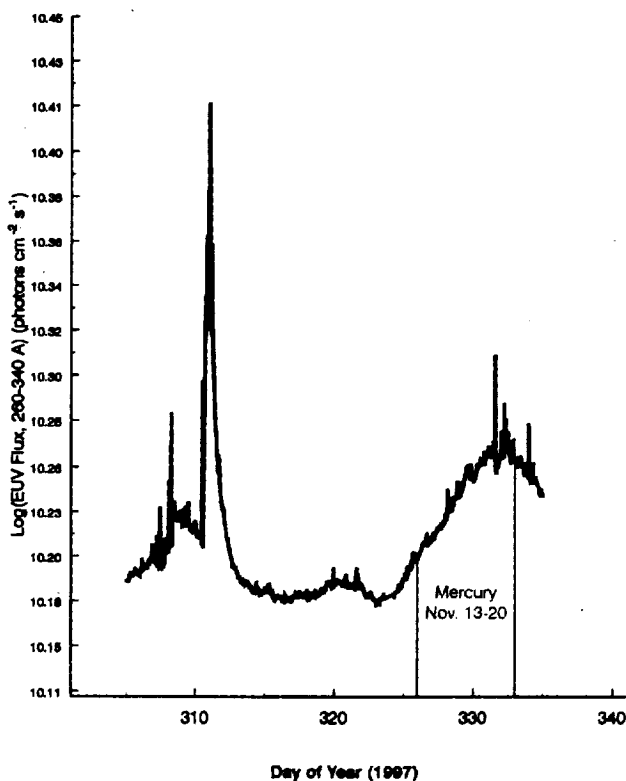
EUV Flux Nov., 1997

Plate 6. The EUV solar flux observed by the SEM experiment on board SOHO. Assuming that the source of radiation rotates with the Sun, the EUV observed at Earth is that which affected Mercury 8.5-9 days earlier. Although the flux at Mercury would be larger by a factor of 5 (November 13) to 5.6 (November 20), the trend seen during our observations is marked on the plate. Our effective solar flux was scaled to the EUV flux and to heliospheric distance.
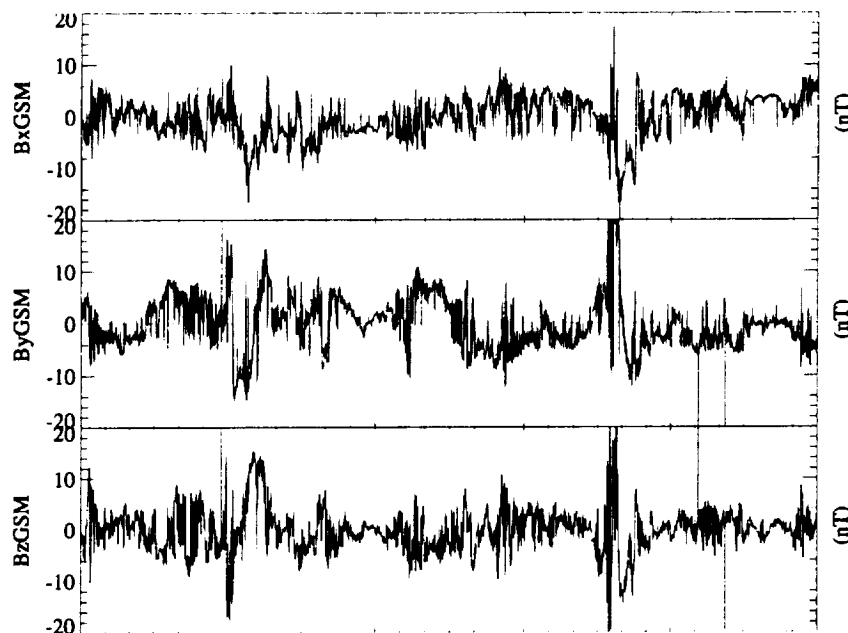
Figure 4. The x, y, and z components of the IMF at Earth for November 1997. The magnitude of the IMF from the quiet Sun scales as R^{-2}, with R the radial heliocentric distance, and follows the Parker spiral. However, impulsive events will have larger effects at Mercury both because of its proximity to the Sun and because of its lower ecliptic latitude.

In addition to the solar wind density and velocity, the magnitude and direction of the interplanetary magnetic field [IMF] at Mercury are required to determine the locus of open field lines to the surface. Because Mercury was near the heliospheric current sheet during our observations, where the z component of the IMF varies rapidly, we were not confident in our ability to predict the IMF at Mercury. The IMF at Earth is shown in Figure 4. Because Mercury is both closer to the Sun and near the plasma sheet, the IMF at Mercury will be both larger in magnitude and more variable. The direction of B_x controls the north-south asymmetry, the value of B_y controls the longitude of the open field lines relative to the subsolar point, and the value of B_z controls the latitude of the open field lines. We show in Figure 5 the effect of varying B_z from +5 nT through 0 nT to -5 nT and in Figure 6 the lesser effect of varying the solar wind dynamic pressure between the minimum and maximum on the days of interest. For these simulations, B_x=-15 nT. It is clear that large areas of the surface will be open to the solar wind even for moderate excursions of the IMF. We list in Table 4 the coordinates of open field lines used in each simulation.

The sputter yield per ion is taken from Flavill et al. [1980]. The measured yield for 400 km s^{-1} H$^+$, He^{2+}, and heavy ions is 1/24, 0.3, and 10, respectively. We took a weighted average yield assuming 95% H, 4% He and 1% heavy ions. We used

an average ionsputter yield of 0.15 per incident solar wind ion, consistent with measured rates. The sputter yield for ions is roughly proportional to the ion energy and can be 2 orders of magnitude larger than the average used here [Johnson, 1990]. Flavill et al. [1980] show that sputter yields can be enhanced up to a factor of 3.5 by the production of needle-like structures which effectively greatly increase the exposed surface area; however, we did not scale the measured sputter yields. We assume that the flux tube cross-sectional area that maps onto the surface is four times the surface area connected to open field lines, consistent with the ratio of the cross-sectional area of the magnetosphere to the cross section of the planet and with 25% penetration of the IMF.

3.2. Photon-Stimulated Desorption

Photon-stimulated desorption was the first mechanism proposed as the major source of the Mercurian atmosphere [McGrath et al., 1986]. The distribution of Na at the Moon, which is peaked at the subsolar point [Flynn and Mendillo, 1995], and at times at Mercury [Killen et al., 1990] seems to be consistent with this source process. The results of McGrath et al. [1986] were criticized because they used PSD yields based on atmospheric ionization rates. More recently, laboratory measurements have been made of PSD yields from

Table 4. Coordinates of Open Field Lines Used in Simulations

Date	Nlat1	Nlat2	Nlong1	Nlong2	Slat1	Slat2	Slong1	Slong2
Nov. 13	00	00	00	00	00	00	00	00
Nov. 14	50	50	-30	30	30	48	-30	30
Nov. 15	40	50	-30	30	20	60	-30	30
Nov. 16	20	65	-30	30	00	00	-00	00
Nov. 18	00	00	00	00	00	20	-30	30
Nov. 20	00	10	-20	20	10	35	-20	20

Figure 6. The effect of solar wind dynamic pressure on the locus of open field lines onto the surface of Mercury from the *Sarantos* [2000] model for $B_z=0$, with (a) pressure P1 as measured on November 13 and (b) pressure P2 as measured on November 20 used in the calculations. The increase in pressure of almost a factor of 2 leads to a small decrease in the extent of the open region and results in the open field lines moving poleward and eastward. The open zones appear at moderate latitudes centered at ~50°.
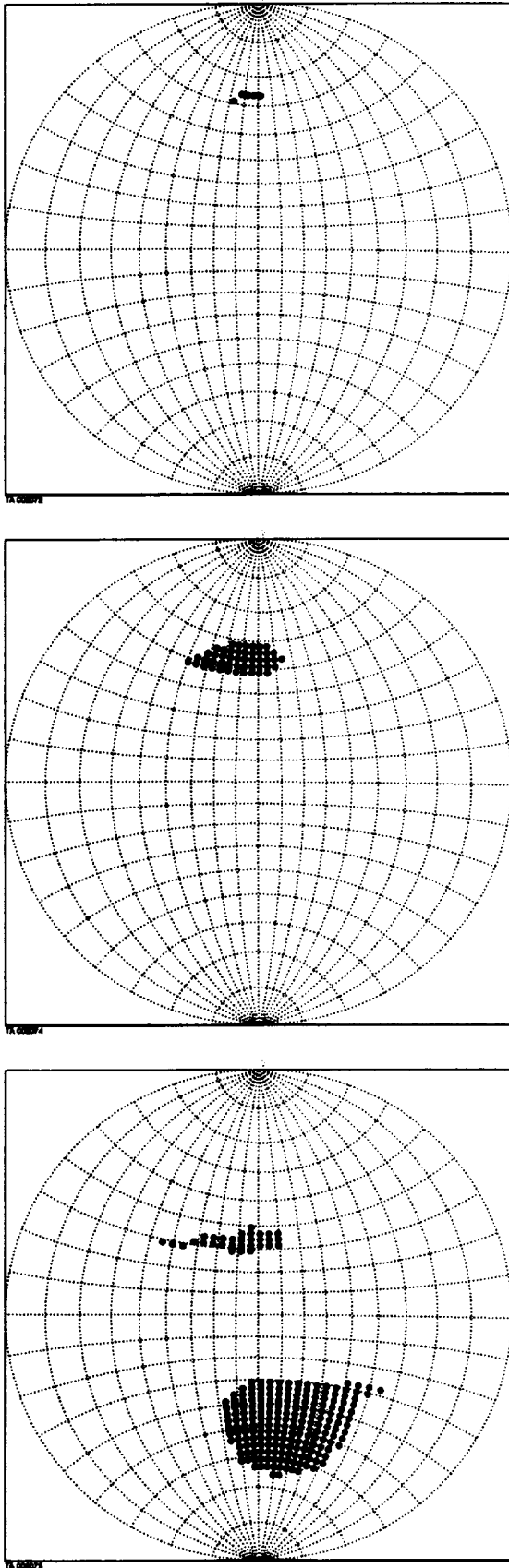
Figure 5. The effect of the z component of the interplanetary magnetic field on the locus of open field lines on the surface of Mercury. B_z was set to (top) +5 nT, (middle) 0 nT, and (bottom) -5 nT. The *Sarantos* [2000] model of the open magnetosphere was used in these calculations.
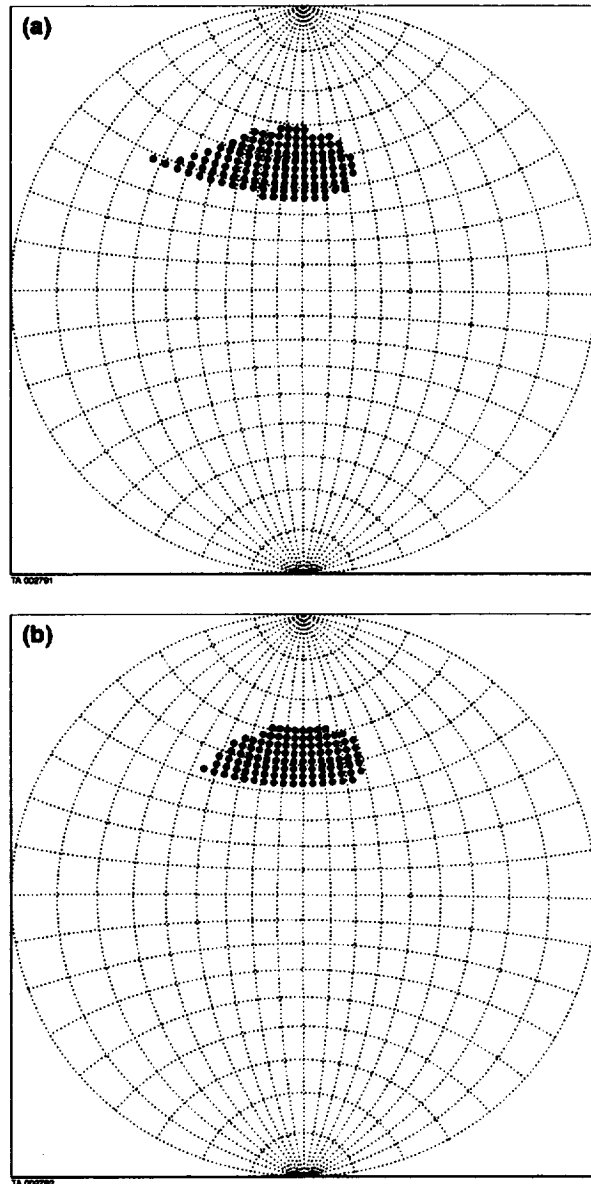
simulated lunar soils [*Yakshinskiy and Madey*, 1999]. For these measurements, sodium was vapor deposited on amorphous stoichiometric SiO_2 films prepared by evaporation of Si in an oxygen atmosphere onto a single Re crystal. The PSD cross section Q was measured at Q~[3±1] x 10^{-20} cm^2 at hv =5 eV [λ=2479 A].

The laboratory-measured PSD yields [*Madey and Yakshinskiy*, 1997; *Madey et al.*, 1998; *Yakshinskiy and Madey*, 1999] are too large to reproduce the measured abundance on the first day of observations [November 13]. There is evidence that the source rate from a planetary regolith must be smaller than that measured in the laboratory for several reasons. First, a regolith has a structure that will trap sputter products before they escape into the atmosphere

Table 5. Solar Flux and Sunspot Numbers

Date	2800 MHz	Sunspot #	EUV flux photon $cm^{-2}s^{-1}1x10^{10}$	Scaling Factor A
Nov. 13	88.2	26	1.58	1.50
Nov. 14	91.0	40	1.62	1.54
Nov. 15	94.1	35	1.66	1.58
Nov. 16	94.1	37	1.70	1.62
Nov. 17	92.0	42	1.74	-
Nov. 18	89.4	46	1.78	1.69
Nov. 19	96.8	45	1.82	-
Nov. 20	86.5	42	1.87	1.77

[Hapke and Cassidy, 1978], and second, the exposed regolith will become depleted in volatiles because of long-term bombardment. We scaled the PSD yields to reproduce the measured sodium abundance on November 13 without ion sputtering to obtain $Q=1.4x10^{-21}$.

We assume that the PSD yield scales as the cosine of the solar zenith angle, and that the flux of photons effective for PSD is 10^{14} A/R_{orb}^2, where A is a factor to account for the solar cycle and the EUV flux (Table 5). We scaled to the EUV flux measured by the Charge, Element and Isotope Analysis System (CELIAS) Solar EUV Monitor (SEM) experiment on board the Solar Heliospheric Observatory (SOHO).

The Lyman alpha flux was generally increasing, beginning early 1996. There was at most a 5% increase in the Lyman alpha flux observed by the Solar Ultraviolet Spectral Irradiance Monitor (SUSIM) instrument on board UARS over the week of our observations, at about the daily fluctuation level. However, there was an 18% increase in the EUV flux (260-340 A) measured by the SEM instrument on board SOHO (Plate 6). The photons in this wavelength range have energies between 47.67 and 36.45 eV, compared with 10 eV at Lyman alpha. Note that the EUV flux was assumed to rotate with the Sun at the solar rotation period, 27.6 days, and therefore affected Mercury some 8-9 days earlier. Therefore our observations were during the period that Mercury was experiencing the gradual rise in EUV flux which was measured at Earth DOY 326 - 332 (November 22-28). Thus the EUV flux seen at Mercury during our observations increased from $1.58x10^{10}$ photons cm^{-2} s^{-1} on November 13 to $1.9x10^{10}$ on November 20, a 20% increase. The EUV flux at Mercury, along with Sunspot number and 2800 MHz flux and the scaling factor A taken from the EUV data are given in Table 5.

3.3. Impact Vaporization

The impact vaporization calculations employed in our model are based on the cratering mechanics of Melosh [1989], specifically, the planar impact approximation (chapter 4). Details of our impact vapor code are given by Morgan and Killen [1998] and are briefly summarized in Appendix C. The rate of meteoritic vaporization of a regolith depends on the volume density of meteoritic material in space at Mercury's orbital distance, the velocity distribution of the meteoroids, Mercury's mass, orbital velocity regolith density, and the meteoroid density. We assume that the velocity distribution of micrometeors is independent of mass and that the micrometeoritic flux is constant over the surface. We calculate the volume of regolith volatilized by assuming that

the threshold pressure associated with 80% devolatilization is 26 GPa [Tyburczy et al., 1986], and we integrate over all velocities such that $P[V_i]>26$ GPa.

Derivation of the transformation of the velocity function from Earth to Mercury is given by Morgan et al. [1988] and by Cintala [1992]. The density of meteoritic material at Earth assumed to be $3 x 10^{-16}$ gm cm^{-3} [Love and Brownlee, 1993] and is scaled to orbital distance R_{orb} as $R_{orb}^{-1.4}$. This mass density includes the mass in the range 10^{-9} to 10^{-4} g measured by the Long Duration Exposure Facility. An equal amount is assumed to be in the 1 cm to 10 km size range but is not considered here. Thus the mass per unit area, m_{pera}, falling on a planet at R_{orb} is

$$m_{pera} = \frac{M_t V_{orb}}{4R_{orb}^{1.4}},\qquad(4)$$

where M_t is total mass per unit volume at lunar orbit and the orbital velocity V_{orb} scales as $R_{orb}^{-\frac{1}{2}}$. Thus the mass per unit area falling on the planet scales as orbital distance $R_{orb}^{-1.9}$, neglecting gravitational focusing. We assume a regolith porosity of 0.1, a regolith density of 1.8 g cm^{-3} and a projectile density of 2.8 g cm^{-3} consistent with those of a chondritic meteorite. Model parameters are summarized in Table 6. A comparison of our results with those of previous models is given in Table 7. The model of Morgan et al. [1988] assumed a meteoritic mass density in lunar orbit of $4x10^{-19}$ kg m^{-3}, in comparison to the $3x10^{-19}$ that we used, and they assumed a sodium weight percent in the regolith of 0.01, in comparison to our value of 0.0053, slightly over lunar. In addition, the velocity distribution they used was an average of those of Southworth and Sekanina [1973], Erickson [1968] and Dohnanyi [1966]. We considered both the velocity function of Erickson [1968] and the velocity function used by Cintala [1992]. Differences between our results and those of Cintala [1992] are explained for the most part by our choice of mass influx (a factor of 3 higher than that used by Cintala) and our explicit use of porosity of 0.1. The porosity may be overly conservative since that of the lunar regolith is 0.5 in the upper 15 cm [Heiken et al., 1991]. A porosity of 0.1 increases the vapor yield by a factor of 2 over a porosity of zero.

4. Model

The loss processes for atmospheric sodium on the dayside are photoionization and migration to the nightside. The column zenith abundance at any given position in the atmosphere, N, is given by

$$N=\phi\tau [1 - exp(-T_m/\tau)],\qquad(5)$$

where ϕ is the source rate at that position [the sum of PSD, ion sputtering, and impact vaporization], τ is the photoionization lifetime, and T_m is the migration time to the terminator. The photoionization lifetime assumed is the experimental value from Huebner et al. [1992]. The theoretical lifetime is a factor of 2.7 longer. The controversy over which cross section may be correct is discussed by Combi et al. [1997]. We obtained T_m by running a polynomial through the results given by Smyth and Marconi [1995a]. The equation used is

$$T_m= 13.514 - 8.298z -3.312 cos(z),\qquad(6)$$

Table 6. Definitions, Symbols and Values for Meteoritic Vaporization

Symbol	Definition	Value or equation
P	peak pressure	
v_o^P	impact velocity for onset of vaporization	7.5 km s^{-1}
v_i	impact velocity	
$f(v_i)$	normalized differential mass flux per unit velocity	
P_o	density of undisturbed regolith	1800 kg m^{-3}
R	radius from impact point	
r_p	radius of impactor	
P_{cp}	critical pressure for devolatilization	26 GPa
S_{cp}	radius of region for which P>P_{cp}	
s_{cp}	S_{cp}/r_p	
	meteoroid mass density at Earth orbit	3x10^{-19} kg m^{-3}
dm/dt	meteoritic mass in fall rate	
dσ/dt	meteoritic mass flux	
d_{reg}	distention	
a		0.052 s m^{-1}
b		1.18
c		2
γ		0.247 s km^{-1}

where z is the solar zenith angle in radians and T_m is in hours. We do not consider sticking at the surface to be a loss process since the atoms will rapidly thermally desorb.

5. Results

The simulated images are shown in Plates 7a - 7f. The simulated and observed images agree qualitatively, while the total sodium content agrees within 10%. Using this model, the contribution from impact vaporization to the total sodium column is 20-32% of the total. This portion will, however, be uniform about the planet to first order. Results of our simulations are summarized in Table 8. The total number of sodium atoms in the sunlit hemisphere, N_{meas}, and the total number in the simulation, N_{calc}, are given along with the percentage from each source process.

We assume that the flux of precipitating solar wind particles onto the surface is $S=4\rho vA$, where ρ is the solar wind density, v is the solar wind velocity, and A is the area on the surface connected to open field lines. For the day on which we recorded the largest total amount of sodium in the atmosphere, November 20, we have an area of 7.3x10^{16} cm^2 exposed to the solar wind, a solar wind density of 120 cm^{-2} and a solar wind velocity of 322 km s^{-1}, resulting in a flux of

Table 7. Comparison Between Results of Various Models for Impact Vaporization of the Regolith of Mercury

Model	Projectile-Target	Vaporization Rate, g cm^{-2} s^{-1}
Morgan et al. [1988]	combination	1.74x10^{-15} aphelion
		6.42x10^{-15} perihelion
Cintala [1992]	diabase-regolith	8.18x10^{-16} aphelion
		2.75x10^{-15} perihelion
This model	diabase-regolith	6.33x10^{-15} aphelion
		1.60x10^{-14} perihelion
This model	diabase-regolith	8.99x10^{-16} aphelion
Erickson [1968] distribution		3.02x10^{-15} perihelion

alpha particles to the surface of 1-4x10^{25} s^{-1}. In contrast, by scaling an Earth magnetosphere model, Goldstein et al. [1981] estimated a maximum flux of alpha particles precipitating onto open field lines of 9x10^{23} s^{-1}. They also scaled the solar wind flux onto the surface by a factor of 4 from the value in the corresponding flux tubes outside the magnetopause.

Impact vaporization consistently produces about a quarter of the source flux, but ion sputtering appeared to increase from noncontributing on November 13 to an important process (32%) on November 20. Photon-stimulated desorption is consistently the dominant source process for this data set.

6. Discussion

By using a scaled version of an Earth magnetosphere model, Goldstein et al. [1981] concluded that the solar wind impacts the surface of Mercury at most 6% of the time, while we conclude that Mercury's magnetosphere is open to the solar wind quite often, at times exposing a large portion of the surface to direct bombardment. Our maximum flux onto the surface is about an order of magnitude larger than that of Goldstein et al. [1981] because we are using an open magnetosphere model. In comparison, our flux estimates do not seem unreasonable. McGrath et al. [1986] estimate a proton flux in auroral zones to be 10^8 - 10^9 cm^{-2} s^{-1} and onto

Table 8. Measured and Calculated Sodium Content of the Hermean Atmosphere

Date	N_{meas} x10^{28}	N_{calc} x10^{28}	% PSD	% ION	% Vapor
Nov. 13	1.1	1.4	68	0	32
Nov. 14	1.4	1.5	64	7	29
Nov. 15	2.0	1.8	59	15	26
Nov. 16	1.5	1.6	64	9	27
Nov. 18	2.0	2.0	60	15	25
Nov. 20	3.1	3.2	48	32	20

the surface along open field lines [cusps] to be about 1.5×10^8 cm^{-2} s^{-1}. Using our estimate for the maximum area exposed to open field lines, 7.3×10^{16} cm^2, we obtain a total sodium content from ion sputtering of 10^{28} using the McGrath et al. [1986] flux and efficiency. If McGrath et al. [1986] had assumed a solar wind density of 120 cm^{-3} instead of 50 cm^{-3}, and assumed a fourfold increase in the flux tube area mapping onto a unit area of surface, their estimate of ion-sputter Na content would increase to 10^{29}, an order of magnitude larger than measured. The average Na column abundance over the sunlit hemisphere resulting from PSD was estimated by McGrath et al. [1986] to be 2×10^{10} - 2×10^{11}. Our average value is about 6×10^9, or about one third of their lower limit. Although we used a higher value for the sodium concentration 0.0053 compared to 0.002 used by McGrath et al. [1986], we also used a lower surface density for the regolith, 7.5×10^{14} atoms cm^{-2}, compared to 2×10^{15}, so that our surface number density is the same. We used a longer lifetime against photoionization, 1×10^4 s, consistent with the experimental value [Huebner et al., 1992], compared to 1×10^3 s used by McGrath et al. [1986]. The major difference is the solar flux times the cross section for sputtering: our value is 1.7×10^{-7}. McGrath et al. [1986] used 10^{-4}, giving a value of Q_{phot} of 10^{-19} if the solar flux is 1.5×10^{14} /R_{orb}^2 cm^{-2} s^{-1}, or 10^{15} at $R_{orb}=0.385$. This cross section is an order of magnitude larger than that measured by Yakshinskiy and Madey [1999] and 2 orders of magnitude larger than that which we used. These differences account for the differences in our estimates.

Potter et al. [1999] have suggested that PSD is not a primary source process in that it promotes only those atoms into the exosphere that are in a physically adsorbed state (as opposed to chemically bound). This is consistent with a lower desorption rate for a weathered surface.

Goldstein et al. [1981] estimate the area in the auroral zones to be 1.9×10^{16} cm^2, comparable to the area we estimate connected to open field lines on a moderately active day. We have not explicitly considered sputtering in auroral zones (i.e., on the nightside). If Mercury's auroral zones are located between 23° and 35° latitude on the nightside, it is not likely that they would contribute to high-latitude enhancements on the dayside.

Caloris basin, the most prominent geologic feature imaged by Mariner 10, centered at +30°, 195°W [Pike, 1988], is the largest impact basin in the solar system. It has been suggested as the source of enhanced flux of both potassium and sodium into the atmosphere of Mercury [Sprague et al., 1990, 1998]. Caloris basin was observed from Earth on each of the days November 13-20, 1997. Mercury rotates slowly because of its 3/2 spin/orbit coupling: it rotates three times for each two orbits about the Sun with an orbital period of 87.9 days and a rotational period of 58.646 days. On November 13 one edge of the basin corresponded roughly to the terminator and the other edge corresponded to the sub-Earth longitude. On November 20 the center longitude of the basin was 8° [¼ of the basin diameter] east of the sub-Earth longitude. The sub-Earth longitude varied by 33° during this observing period, approximately the diameter of Caloris basin (31° across, stretching from 15°N to ~ 45° north latitude). The approximate position of Caloris basin relative to the subsolar and sub-Earth points is shown in Figure 2. The basin rotated toward the subsolar point during the week of observations, starting 67° from the subsolar longitude on November 13 and ending 46° from the subsolar longitude on November 20.

In order to test the hypothesis that Caloris basin is responsible for atmospheric enhancements [Sprague et al., 1990, 1998], we modeled the sodium abundance as doubled in the Caloris basin region. This resulted in a maximum 10% effect, too small to account for the threefold increase in atmospheric sodium or the location of the enhancements. However, we demonstrate that the resulting effect would be visible, as seen on the simulations. If the source rates from the Caloris region were enhanced by even a factor of 2 over adjacent terrain, the resulting enhancements would be easily observed. These enhancements do not appear in our observations.

7. Conclusions

Magnetospheric models have shown that Mercury's magnetosphere is probably open to the solar wind over substantial areas when the IMF turns southward [Luhmann et al., 1998; Sarantos, 2000]. We show that ion sputtering in regions open to solar wind bombardment can cause the transient variations seen in Mercury's atmosphere. We conclude that impact vaporization is the least important but nevertheless a substantial source process for atmospheric sodium and that PSD can supply the atmosphere during magnetically quiet times. Because the IMF at Mercury is unknown during the times of our observations, we can only conclude that plausible variations in the magnetosphere are consistent with the hypothesis that rapid changes in Mercury's exosphere are due to ion sputtering in regions where the field lines are open to the surface. Although we conclude that PSD produces the bulk of the sodium in the atmosphere when there is no magnetic reconnection, we also conclude that ion sputtering can at times produce a comparable source rate.

Appendix A: Data Calibration -- Calculation of Na D$_2$ Intensity

The continuum reflected from the surface, F_s, is given by

$$F_s = \frac{R}{\Pi} \frac{F}{D^2}, \tag{A1}$$

where R is the Hapke reflectivity, F is Solar flux in the continuum near the line, and, D is distance from the Sun in AU. If the pixel size is S [steps/Å], then the equivalent width of the line, W, is given by

$$W = \frac{C_{Na}}{S C_{Continuum}}, \tag{A2}$$

where C_{Na} is the integrated counts in the sodium line and $C_{continuum}$ is the counts/step in the continuum.

Then the irradiance in the sodium line is given by

$$4\pi I[\text{Na}] = 4\Pi \left[\frac{R}{\Pi} \frac{F}{D^2} \frac{C_{Na}}{C_{Cont} S} \right], \tag{A3}$$

where 4π converts intensity to irradiance (steradians), R is Hapke bidirectional reflectivity, F is Solar flux, D is orbital distance in AU, C_{Na} is integrated counts in the D line, C_{Cont} is counts per step in the continuum, and S is steps/Å.

N   log N (cm⁻³)   10.88   N   log N (cm⁻³)   11.06
                                     10.25   10.37
                                      9.62   9.68
                                      9.00   9.00

                    E   E

            Nov. 13,1997   Nov. 14,1997

N   log N (cm⁻³)   11.06   N   log N (cm⁻³)   11.07
                                     10.37   10.38
                                      9.68   9.69
                                      9.00   9.00

                    E   E

            Nov. 15,1997   Nov. 16,1997

N   log N (cm⁻³)   11.33   N   log N (cm⁻³)   11.58
                                     10.55   10.72
                                      9.77   9.86
                                      9.00   9.00

                    E   E

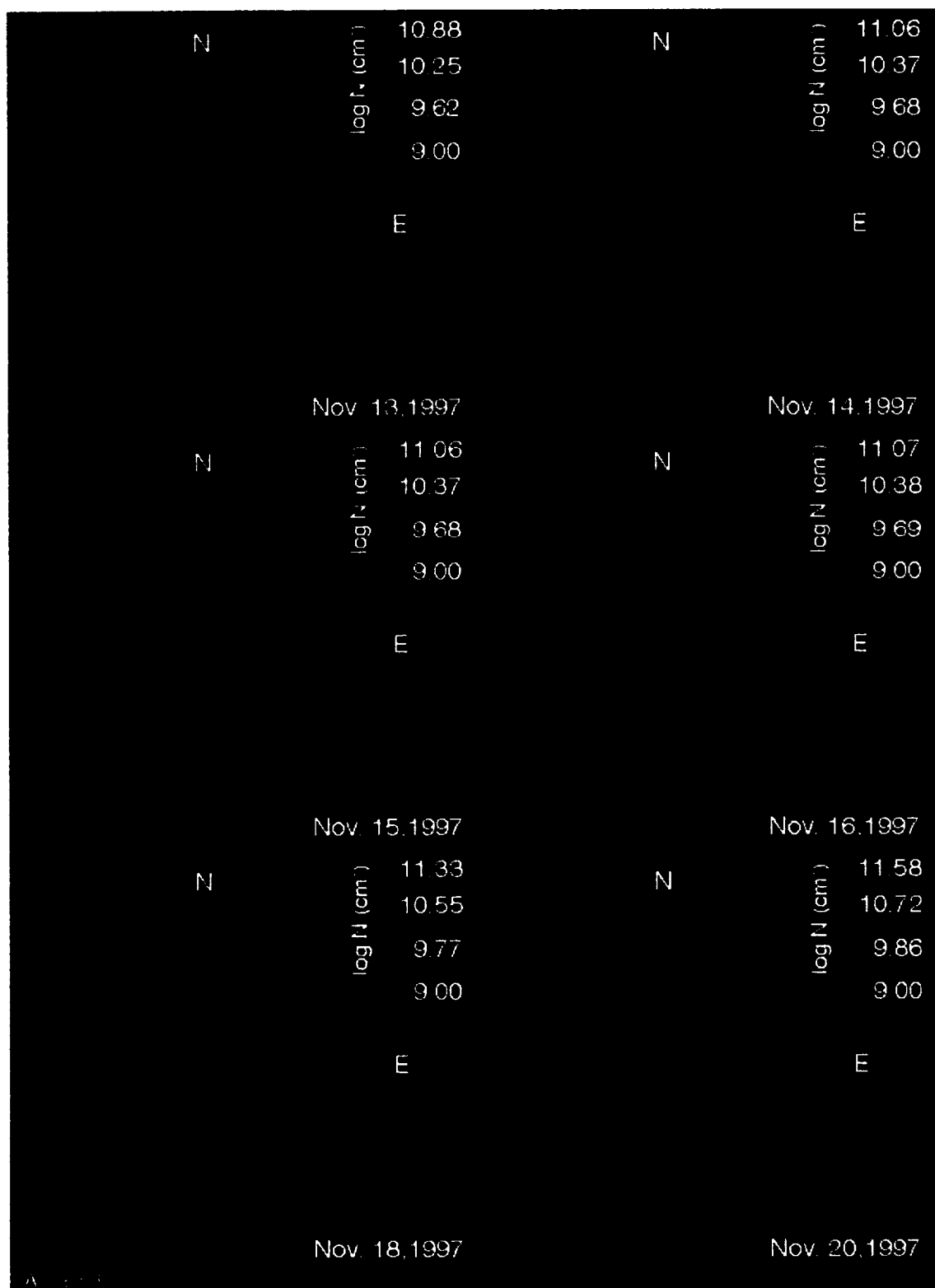   Nov. 18,1997   Nov. 20,1997

Plate 7. Simulated observations of the sodium atmosphere for November 13-20, 1997, at quarter phase. The color code is log(number density (cm⁻²)). North is at the top, and west is to the left. Caloris basin is modeled with doubled sodium content and can be faintly seen in the northern hemisphere. There is no feature in the data corresponding to the position of Caloris basin.

Appendix B

The radiative transfer is based on the method detailed by *Killen* [1988]. The total intensity in the line (in Rayleighs) is given by

$$4\pi I(\tau_0, \nu) = \frac{\gamma \pi F_c}{R_m^2} \int_{-\infty}^{\infty} \Phi(T_0, \nu) d\nu , \qquad (B1)$$

where πF_c is the solar flux in the continuum near the D line, γ is the fraction of the continuum at the line center as seen by an atom at rest in Mercury's atmosphere, and R_m is Mercury's instantaneous orbital distance. Since Mercury's orbital eccentricity is 0.2, the residual solar flux in the solar Fraunhofer line seen by an atom in Mercury's atmosphere varies about the orbit from the minimum (0.049 at D_2, 0.0555 at D_1) to a maximum of 0.44 at D_2, and 0.53 at D_1 [e.g., *Smyth and Marconi* 1995a Figure 4]. We have taken the solar flux in the continuum at D_2 to be $\pi(217.3)$ photons cm^{-2} s^{-1} Hz^{-1}. The line profile of the scattered light is given by

$$\Phi(\tau_0, \nu) = \frac{\varpi \mu_0}{\mu + \mu_0}[X(\tau_\nu, \mu_0)X(\tau_\nu, \mu_0) - Y(\tau_\nu, \mu)Y(\tau_\nu, \mu_0)] \qquad (B2)$$
$$+ \frac{4\pi R \gamma_1(\mu)}{(1 - \pi R_s)},$$

where μ and μ_0 are the cosines of the emergence and incidence angles, respectively, and the single-scattering albedo is unity; τ_0 is the optical depth in the line center. The X and Y functions are scattering functions [*Chandrasekhar*, 1960; *Dunn et al.*, 1982]. The second term is the ground reflectance scattered by the atmosphere and is small since the planetary reflectance is 0.04. It is included except for off-limb viewing. The term R is the Hapke reflectance function [e.g., *Hapke*, 1984]. We used the empirical parameters $\theta_b = 21°$, $h_t = 0.11$, and surface albedo $\omega_{surf} = 0.2$ [*Domingue et al.*, 1997].
The additional functions,

$$\gamma_1(\mu) = \frac{1}{2}\varpi_0\beta_0 X(\mu) + \frac{1}{2}(2 - \varpi_0\tau_0)Y(\mu), \qquad (B3)$$

$$\overline{S} = 1 + Q(\tau_1 + \beta_1)^2, \qquad (B4)$$

$$Q = -(\tau_1 - \beta_1)/[(\tau_1 + \beta_1)\tau_2 + 2(\tau_2 + \beta_2)], \qquad (B5)$$

are given by *Chandrasekhar* [1960] for the planetary problem for conservative, isotropic scattering.
The value of μ_0 is the cosine of the solar zenith angle. For limb viewing, μ is set to 0.2, satisfying the integrated tangent column for T=1100 K:

$$N_{tan} = n(r)H\left[\frac{2\pi r}{H}\right]^{1/2}\left[1 + \frac{3}{8}\frac{H}{r}\right] \qquad (B6)$$

[*Chamberlain* and *Hunten*, 1987], where $H = KT/mg$ is the scale height for a barometric atmosphere and r is the planetary radius to the tangent point. Because of curvature, the maximum value of μ is 0.2. The opacity is computed in the a and b components of each sodium line separately. The total optical depth at a given frequency is the sum of the two components. Up to three thermal components are allowed in the model. The relative opacities in the center of the components before summation are 1, 0.59866, 0.4849, and 0.2954 at $D_2(a)$, $D_2(b)$, $D_1(a)$, and $D_1(b)$, respectively.

The input parameter is the optical depth in the line center of $D_2(a)$ (before summation). Then,

$$\tau_\gamma = \Sigma_{i,j}\tau_{0i,j}\exp\left[-\frac{[\nu - \nu_0(i)]^2}{\Delta\nu_0(i)^2}\right], \qquad (B7)$$

where i represents the a or b component [fine structure] and j represents the thermal component (up to three temperatures). The Doppler width is $\Delta\nu_D = u\nu/c$, and $\bar{u} = \sqrt{2kT/m}$ is the most probable velocity of a Boltzmann distribution.

Appendix C: Impact Vaporization

The radius of the devolatilized region [s_{cp}] in units of impactor radius is

$$s_{cp}(v_i) = \left\{\frac{0.29 \times 26}{P_p(v_i)}\right\}^{av_i + b} - c, \qquad (C1)$$

where constants a, b, and c are 0.052 s m^{-1}, 1.18, and 2, respectively. The constants b and c are unitless. $P_p[V_i]$ is the peak pressure at the impact in GPa, and P_{cp} is the critical pressure for devolatilization if $P_{cp}[v] > 26$ GPa. Note that this is less for a regolith than for a solid rock, for which v_{min} is 16-25 km s^{-1}. We obtain the vaporization source rate per unit area per unit time, $d\sigma/dt$, by integrating $s_{cp}^3[P_{cp}]$ over the velocity function for incoming meteoroids, $f(v_i)$:

$$\frac{d\sigma}{dt} = \frac{1}{8}\left(\frac{\rho_{reg}}{\rho_p}\right)\frac{dm}{dt}\{s_{cp}(P_{cp})\}^3 f(v_i)dv_i, \qquad (C2)$$

where ρ_{reg} is the regolith density, ρ_p is the impactor density, and P_{cp}, S_{cp} and $f(v_i)$ all depend on v_i. We assume that $v_{max} = 116.4$ km s^{-1}. The minimum velocity required to completely vaporize the shocked target is 11.45 km s^{-1}, given that this requires a shock stress of 236.1 GPa [Cintala, 1992]. We integrated over the velocities from 7.5 to 116.4 km s^{-1}. The results do not depend critically on v_{min}. The velocity functions assumed are given below.
Let M_t be the mass of meteoritic material per cubic centimeter at Earth orbit. The mass density varies with orbital distance R as $R^{-1.4}$ and velocity varies as $R^{-1/2}$. Then the average mass flux, M_{pers}, over the planet's surface is

$$M_{pers} = \frac{M_t V}{4R^{1.9}}, \qquad (C3)$$

where V is the relative orbital velocity of the meteoroid in orbit at the Moon.
We use a meteoroid mass density at 1 AU, $M_t = 3.0 \times 10^{-16}$ g cm^{-3}, which includes mass density of micrometeoroids 10^{-9} to 10^{-4} g. An equal mass of meteoroids in the 1 cm to 10 km size range [*Love and Brownlee*, 1993] is not included in the calculation. There is a factor of at least 2 uncertainty in the calculation owing to uncertainty in both the mass density and the velocity distribution at Mercury's orbit.
The velocity distribution at Mercury's surface, F_m (V_m), is given by [*Morgan et al.*, 1988]

$$F_m(V_m) = K_2[R]R^2 \left\{ \frac{\left[V_1^2/r + V_{em}^2 \right]^{1/2}}{V_1} \right\}^3 \left(\frac{V_1}{V_e} \right)^3 f_e(V_e), \quad (C4)$$

where $f_e(v_e) = k \exp(-\gamma u)$, k and K_2 are normalizing constants, $\gamma=0.247$, $u=\{r[v_m^2 - v_{em}^2] + v_{ee}^2\}^{1/2}$, v_{em} is the escape velocity at Mercury, r is Mercury's orbital distance in AU, V_m is the velocity at Mercury's surface, V_1 is the particle's velocity in space at 1 AU (far from the gravitational influence of the Earth), and V_e is the velocity of a particle at the base of Earth's atmosphere.

References

Asai, K. M. Kojima, M. Tokumaru, A. Yokobe, B.V. Jackson, P.L. Hick, and P.K. Manoharan, Heliospheric tomography using interplanetary scintillation observations, 3. Correlation between speed and electron density fluctuations in the solar wind. *J. Geophys. Res., 103,* 12,049, 1998.

Baker, D.N., J.E. Borovsky, J.O. Burns, G.G. Gisler, and M. Zeilik, Possible calorimetric effects at Mercury due to solar wind-magnetosphere interaction,. *J. Geophys. Res., 92,* 4704, 1987.

Bida, T.A., R.M. Killen, and T.H. Morgan, Discovery of calcium in Mercury's atmosphere, *Nature, 404,* 159, 2000.

Broadfoot, A.L., D.E. Shemansky, and S. Kumar, Mariner 10: Mercury atmosphere, *Geophys. Res. Lett., 3,* 577, 1976.

Chamberlain, J.W., and D.M. Hunten, *Theory of Planetary Atmospheres,* Academic, San Diego, California, 1987.

Chandrasekhar, S., *Radiative Transfer,* Dover, New York, 1960.

Cheng, A.F., R.E. Johnson, S.M. Krimigis, and L.J. Lanzeroti, Magnetosphere, exosphere and surface of Mercury. *Icarus, 71,* 430, 1987.

Cintala, M.J., Impact-induced thermal effects in the lunar and Mercurian regoliths. *J. Geophys. Res., 97,* 947, 1992.

Combi, M.R., M.A. DiSanti and U. Fink, The spatial distribution of gaseous atomic sodium in the comae of comets: Evidence for direct nucleus extended plasma sources, *Icarus, 130,* 336, 1997.

Dohnanyi, J.S., Model distribution of photographic meteors, *Bellcom TR-66-340-1,* Bellcom Inc., Washington, D.C., 1966.

Domingue, D.L., A.L. Sprague, and D.M. Hunten, Dependence of Mercurian atmospheric column abundance estimations on surface reflectance modeling, *Icarus, 128,* 75, 1997.

Dunn, W.L., R.D.M. Garcia, and C.E. Siewert, Concise and accurate solutions for Chandrasekhar's X and Y functions, *Astrophys. J., 260,* 849, 1982.

Erickson, J.E., Velocity distribution of sporadic meteors, *J. Geophys. Res., 73,* 3721, 1968.

Flavill, R.P., W.C. Carey, J.A.M. McDonnell, D.G. Ashworth, and R.J. Allison, Progress in defining the solar wind sputter rate on protoplanets and interplanetary matter, *Planet. Space Sci., 28,* 511, 1980.

Flynn, B., and M. Mendillo, Simulations of the lunar sodium atmosphere, *J. Geophys. Res., 100,* 23,271, 1995.

Goldstein, B.E., S.T. Suess, and R.J. Walker, Mercury: Magnetospheric processes and the atmospheric supply and loss rates, *J. Geophys. Res., 86,* 5485, 1981.

Hapke, B., Bidirectional reflectance spectroscopy, 3, Correction for macroscopic roughness, *Icarus, 59,* 41, 1984.

Hapke, B., and W.A. Cassidy, Is the Moon really as smooth as a billiard ball? Remarks on models of sputtering of the lunar surface, *Geophys. Res., Lett.,* 5, 297, 1978.

Hapke, B., G.E. Danielson, K. Klaasen, and L. Wilson, Photometric observations of Mercury from Mariner 10, *J. Geophys. Res., 80,* 2431, 1975.

Heiken, G.H., D.T. Vaniman, and B.M. French, *Lunar Sourcebook,* Cambridge Univ. Press, New York, 1991.

Hick, P., and B.V. Jackson, Solar wind mass and momentum flux variations at 0.3 AU, *Adv. Sp. Res., 14* (4), 139, 1994.

Huebner, W.F., J.J. Keady, and S.P. Lyon, Solar photo rates for planetary atmospheres and atmospheric pollutants, *Astrophys. Space Sci., 195,* 1, 1992.

Hunten, D.M., R.W.H. Kozlowski, and A.L. Sprague, A possible meteor shower on the Moon, *Geophys. Res. Lett., 18,* 2101, 1991.

Hunten, D.M., G. Cremonese, A.L. Sprague, R.E. Hill, S. Verani, and R.W.H. Kozlowski, The Leonid meteor shower and the lunar sodium atmosphere, *Icarus, 136,* 298, 1998.

Ip, W.-H., The sodium exosphere and magnetosphere of Mercury, *Geophys. Res. Lett., 13,* 423, 1986.

Ip, W.-H., Dynamics of electrons and ions in Mercury's magnetosphere, *Icarus, 71,* 441, 1987.

Ip, W.-H., On solar radiation-driven surface transport of sodium atoms at Mercury, *Astrophys. J., 356,* 675, 1990.

Jackson, B.V., P.L. Hick, and A. Yokobe, Heliospheric tomography using interplanetary scintillation observations, *Adv. Sp. Res., 20* (1), 23, 1997a.

Jackson, B.V., P.L. Hick, and A. Yokobe, Heliosphere tomography using interplanetary scintillation parameters, *Phys. Chem. Earth, 22,* 425, 1997b.

Jackson, B.V., P.L. Hick, and A. Yokobe, Heliospheric tomography using interplanetary scintillation observations, 1. Combined Nagoya and Cambridge data, *J. Geophys. Res., 103,* 12,049, 1998.

Johnson, R.E., *Energetic Charged-Particle Interactions With Atmospheres and Surfaces,* 232 pp., Springer-Verlag, New York, 1990.

Kabin, K., T.I. Gombosi, D.L. DeZeeuw, and K.G. Powell, Interaction of Mercury with the solar wind, *Icarus, 143,* 397, 2000.

Killen, R.M., Resonance scattering by sodium in Mercury's atmosphere 1. The effect of phase and atmospheric smearing, *Geophys. Res. Lett., 15,* 80, 1988.

Killen, R.M., A.E. Potter, and T.H. Morgan, Spatial distribution of sodium vapor in the atmosphere of Mercury, *Icarus, 85,* 145, 1990.

Killen, R.M., A.E. Potter, A. Fitzsimmons, and T.H. Morgan, Sodium D2 line profiles: Clues to the temperature structure of Mercury's exosphere. *Planet. Space Sci., 47,* 1449, 1999.

Love, S.G., and D.E. Brownlee, A direct measurement of the terrestrial mass accretion rate of cosmic dust, *Science, 262,* 550, 1993.

Luhmann, J.G., C.T. Russell, and N.A. Tsyganenko, Disturbances in Mercury's magnetosphere: Are the Mariner 10 "substorms" simply driven?, *J. Geophys. Res., 103,* 9113, 1998.

Madey, T.E., and B.V. Yakshinskiy, Desorption of Na from model mineral surfaces: Relevance to origins of Na in the atmospheres of Mercury and the Moon, *Bull. Am. Astron. Soc., 29*(3), 1307, 1997.

Madey, T.E., B.V. Yakshinskiy, V.N. Ageev, and R.E. Johnson, Desorption of alkali atoms and ions from oxide surfaces: relevance to origins of Na and K in the atmospheres of Mercury and the Moon, *J. Geophys. Res., 103,* 5873, 1998.

McGrath, M.A., R.E. Johnson, and L.J. Lanzerotti, Sputtering of sodium on the planet Mercury, *Nature, 323,* 694, 1986.

Melosh, H.J., *Impact Cratering: A Geologic Process,* Oxford Univ. Press., New York, 1989.

Mendillo, M., J. Baumgardner, and J. Wilson, Observational test for the solar wind sputtering origin of the Moon's extended sodium atmosphere, *Icarus, 137,* 13, 1990.

Morgan, T.H., and R.M. Killen, Unsteady diffusive flows in the Mercurian regolith, *Bull. Am. Astron. Soc., 26*(3), 1105, 1994.

Morgan, T.H., and R.M. Killen, Production mechanisms for faint but

possibly detectable coronae about asteroids, *Planet. Space Sci.,* *46,* 843, 1998.

Morgan, T.H., and D.E. Shemansky, Limits to the lunar atmosphere, *J. Geophys. Res., 96,* 1351,1991.

Morgan, T.H., H.A. Zook, and A.E. Potter, Impact-driven supply of sodium and potassium to the atmosphere of Mercury, *Icarus, 75,* 156, 1988.

Pierce, K., Construction of a Bowen image slicer, *Publ. Astron. Soc. Pac., 77,* 216, 1965.

Pike, R.J., Geomorphology of impact craters on Mercury, in *Mercury* edited by F. Vilas, C. Chapman, and M.S. Matthews, pp. 165-273, Univ. Ariz. Press, Tucson, 1988.

Potter, A.E., R.M. Killen and T.H. Morgan, Rapid changes in the sodium exosphere of Mercury, *Planet. Space Sci., 47,* 1441, 1999.

Potter, A.E., R.M. Killen, and T.H. Morgan, Variation of lunar sodium during passage of the Moon through the Earth's magnetotail, *J. Geophys. Res., 105,* 15,073, 2000.

Potter, A.E., and T.H. Morgan, Evidence for suprathermal sodium atmosphere of Mercury, *Adv. Space Res., 19*(10), 1571, 1997.

Potter, A.E., and T.H. Morgan, Discovery of sodium in the atmosphere of Mercury, *Science, 229,* 651, 1985.

Potter, A.E., and T.H. Morgan, Potassium in the atmosphere of Mercury, *Icarus, 67,* 336, 1986.

Potter, A.E., and T.H. Morgan, Evidence for magnetospheric effects on the sodium atmosphere of Mercury, *Science, 248,* 835, 1990.

Richardson, E.H., J.M. Fletcher, and W.A. Grundmann, in *Very large telescopes, their instrumentation and programs, Proceedings of the Colloquium,* Garching, West Germany, April 9-12, 1984 (A85-3692617-89), pp. 469-492; Discussion, p.492, Eur. South. Obs., 1984.

Sarantos, M., An open magnetosphere model for Mercury, Masters thesis, Rice University, Houston, Tex., 2000.

Shemansky, D.E., and T.H. Morgan, Source processes for the alkali metals in the atmosphere of Mercury, *Geophys. Res. Lett., 18,* 1659, 1991.

Smith, S., J.K. Wilson, J. Baumgardner, and M. Mendillo, Discovery of the distant lunar sodium tail after the leonid meteor shower of 1998, *Geophys. Res. Lett., 26,* 1649, 1999.

Smyth, W.H., Nature and variability of Mercury's sodium atmosphere, *Nature, 323,* 696, 1986.

Smyth, W.H., and M.L. Marconi, Theoretical overview and modeling of the sodium and potassium atmospheres of Mercury. *Astrophys. J., 441,* 839, 1995a.

Smyth, W.H. and M.L. Marconi, Theoretical overview and modeling of the sodium and potassium atmospheres of the Moon, *Astrophys. J., 443,* 371, 1995b.

Southworth, R.B., and Z. Sekanina, Physical and dynamical studies of meteors, *NASA Contract. Rep., CR-2316,* 1973.

Sprague, A.L., R.W.H. Kozlowski, and D.M. Hunten, Caloris Basin: An enhanced source for potassium in Mercury's atmosphere, *Science, 249,* 1140, 1990.

Sprague, A.L., W.J. Schmitt, and R.E. Hill, Mercury: Sodium atmospheric enhancements, radar-bright spots, and visible surface features, *Icarus, 136,* 60, 1998.

Stern, S.A., A. Fitzsimmons, R.M. Killen, and A.E. Potter, A direct measurement of sodium temperature in the lunar exosphere, in *Proc. Lunar Sci. Conf. XXXI,* abstract 1122, Houston, Texas, 2000.

Toffoletto, F.R., Model of solar wind magnetosphere coupling, Ph.D. thesis, Rice Univ., Houston, Tex., 1987.

Toffoletto, F.R., and T.W. Hill, A nonsingular model of the open magnetosphere, *J. Geophys. Res., 98,* 1339, 1993.

Tyburczy, J.A., B. Frisch, and T.J. Ahrens, Shock-induced volatile loss from a carbonaceous chondrite - Implications for planetary accretion, *Earth Planet Sci. Lett., 307,* 201, 1986.

Verani, S., C. Barbieri, C. Benn, and G. Cremonese, Possible detection of meteor stream effects on the lunar sodium atmosphere, *Planet. Space Sci., 46,* 1003, 1998.

Voigt, G.H., A mathematical magnetospheric field model with independent physical parameters, *Planet. Space Sci., 29,* 1, 1981.

Wilson, J.K., S.M. Smith, J. Baumgardner, and M. Mendillo, Modeling an enhancement of the lunar sodium tail during the Leonid meteor shower of 1998, *Geophys. Res. Lett., 26,* 1645, 1999.

Yakshinskiy, B.V., and T.E. Madey, Photon-stimulated desorption as a substantial source of sodium in the lunar atmosphere, *Nature, 400,* 642, 1999.

B. Giles, NASA Goddard Space Flight Center, Interplanetary Physics Branch, code 692, Building 2, Room 148, Greenbelt, MD 20771. (barbara.giles@gsfc.nasa.gov)

P. Hick and B. V. Jackson, Center for Astrophysics and space Sciences, University of California, San Diego, 9500 Gilman Drive, La Jolla, CA 92093-0111. (bjackson@cass01.ucsd.edu)

R. M. Killen, Instrumentation and Space Research, Southwest Research Institute, 6220 Culebra Road, P.O. Drawer 28510, San Antonio, TX 78228-0510. (rkillen@swri.edu)

A. E. Potter, National Solar Observatory, Tucson, AZ 85719. (apotter@noao.edu)

P. Reiff and M. Sarantos, Department of Space Physics and Astronomy, Rice University, MS-108, 6100 South Main, Houston, TX 77005. (reiff@spacsun.rice.edu)